Dual confinement of LaCoO$_x$ modified Co nanoparticles for superior and stable ammonia decomposition

Xi Han [a,1], Minghao Hu [a,1], Junchao Yu [a], Xuan Xu [a], Peng Jing [a], Baocang Liu [a,*], Rui Gao [a,*], Jun Zhang [a,b,c,**]

[a] School of Chemistry and Chemical Engineering & Inner Mongolia Engineering and Technology Research Center for Catalytic Conversion and Utilization of Carbon Resource Molecules, Inner Mongolia University, 49 Xilinguole South Road, Hohhot 010020, PR China
[b] Inner Mongolia Academy of Science and Technology, 70 Zhaowuda Road, Hohhot 010010, PR China
[c] Inner Mongolia Guangheyuan Nano High-tech Co. LTD, Ejin Horo Banner, Ordos 017299, PR China

ABSTRACT

In this work, we report the rational design of amorphous LaCoO$_x$ modified Co nanoparticles confined in both nitrogen-doped carbon (NC) matrix and two-dimensional (2D) mesoporous silica (LaCoO$_x$/Co@NC/SBA-15(2D)) via in situ confined pyrolysis of nano-sized La doped ZIF-67 in the mesopores of SBA-15(2D) as a novel dual-spatially-confined composite catalyst with superior activity and stability toward ammonia decomposition to produce hydrogen. It achieves a NH$_3$ conversion efficiency close to 100 % at a high gas hourly space velocity (GHSV) of 60,000 g$_{cat}^{-1}$ h^{-1} with an encouraging H$_2$ production rate of 446 mmol g$_{Co}^{-1}$ min^{-1} at 600 °C and can maintain stable catalytic activity for 200 h, almost outperforming all Co-based catalysts reported so far. Various characterizations and theoretical calculation results reveal that the outstanding ammonia decomposition performance mainly origins from the dual-spatially-confined configuration, fully exposed active sites and high mass transfer efficiency, and the synergy of amorphous LaCoO$_x$, Co nanoparticles and NC matrix.

1. Introduction

As a series of energy and environmental issues caused by the excessive consumption of fossil fuels have caused a huge threat to global sustainable development. Hydrogen has been deemed as an ideal alternative energy carrier to current fossil fuels due to its high energy density, cleanliness, and environmental friendliness [1–3]. Recently, ammonia (NH$_3$), with high hydrogen gravimetric (17.7 wt % H$_2$) and energy density (3000 W·h·kg^{-1}), has been deemed to a promising hydrogen storage medium, and catalytic decomposition of NH$_3$ offers a hopeful route to efficient and clean hydrogen generation [4,5]. Among various catalysts, noble-metal based, especially Ru based catalysts exhibit superior catalytic performance for ammonia decomposition [6–10], while the high price and low abundance limit their large-scale applications. Therefore, it is imperative to develop non-noble metal catalysts with high activity and stability for ammonia decomposition [11,12].

Cobalt-based catalysts, which are recognized as one of the most

active non-precious metal-based ammonia decomposition catalysts, have been attracted great attention [13,14]. However, some inherent drawbacks, including poor low-temperature reaction kinetics and serious sintering problems at high temperatures restrict its low-temperature and long-term usage [15]. Therefore, it is of great significance to exploit efficient methods to improve its low-temperature activity and high-temperature stability for ammonia decomposition. At present, some effective strategies such as adding a promoter, preparing bimetallic alloy or compound, utilizing mesoporous materials to confine metal nanoparticles, using a suitable support, and coating a protective layer have been developed to enhance the ammonia decomposition activity and stability of transition-metal based catalysts [11,16–18].

As an efficient way, using ordered mesoporous materials with high surface area and uniform pore size, such as SBA-15 and KIT-6, as support were proved to be able to suppresses the agglomeration or sintering of active species, improve the dispersibility of active species, and enhance the catalytic activity and stability [11,15,17,19,20]. However, the reported three-dimensional (3D) ordered mesoporous supporting

materials have some inherent shortcomings, such as their limited accessibility of in-pore surface and long mass-diffusion distance, which is unfavorable for the loading and dispersion of active species and the mass-transfer during reaction [21]. Endowing ordered mesoporous support with two-dimensional (2D) structure can significantly increase the numbers of exposed mesopore channels, improve the accessibility of active sites, and shorten mass transfer distances [21,22], which can fully play the advantages of mesoporous support materials, but have been rarely reported. In addition, it is difficult to ensure all active species were incorporated in mesopores, and the residual active species loaded on outside of mesopores may occur agglomeration during reaction at high-temperatures, which would block mesopores and limit mass-diffusion along pores, and leading to a decreased catalytic performance. Recently, encapsulating the metal or metal oxide nanoparticles in N-doped carbon materials by pyrolyzing metal–organic frameworks (MOFs) under an inert atmosphere has been widely used to enhance the stability of metal-based catalysis [23–26]. Therefore, it can be expected that if directly filling MOFs precursors into the pores of 2D ordered mesoporous support materials followed by pyrolyzing, the obtained metal or metal oxide nanoparticles in pore will receive the dual confined effect of channels and carbon materials and the others loaded on the outside of pore channels is also restricted by carbon materials. And the obtained supported catalysts would exhibit enhanced catalytic activity and stability.

As the other important route, adding a promoter can optimize the adsorption process of reactants and intermediates as well as products desorption processes via tuning the surface acidity/alkalinity and the electronic structure of catalyst [27,28]. It has been proved that alkali, alkaline-earth, and several rare earth metals could act as efficient promotors to enhance the catalytic ammonia decomposition performance of transition metal-based nanoparticle catalysts [18,28,29]. Among these promotors, La-based compounds, such as La_2O_3 and $LaCoO_x$ have received special attentions. For example, Hu et al. prepared La species modified MgO catalyst by co-precipitation method and found the introduction of La species can effectively promote the adsorption decomposition of NH_3 and desorption of N_2 thereby enhancing the ammonia decomposition performance, but the authors did not point the existed form of La species. Gao et al. reported an attractive way of La^{3+} doped ZIF-67 derived method to achieve $Co/LaCoO_x$ hybrid nanoparticles embedded in porous nitrogen-doped carbon matrix as a superior electrocatalyst for hydrazine-assisted hydrogen generation, in which the formation of amorphous $LaCoO_x$ species can bring more active sites for surface redox reactions [30].

At the same time, the adsorbed sites in amorphous short-range ordered $LaCoO_x$ can moderately bound nitrogen molecules, and effectively lowers the activation energy of nitrogen desorption. Therefore, it may be beneficial to the surface-sensitive ammonia decomposition reaction [31, 32]. However, although many studies have been performed to give insight into NH_3 decomposition reaction on cobalt surfaces, detailed reaction pathways and catalytic mechanisms of $LaCoO_x$ modified Co-based catalysts have not yet been studied and fully elucidated. In addition, it is still difficult to simultaneously achieve high activity at low-temperature as well good stability at high-temperature for Co-based catalysts by using the present synthesis method.

In this work, we report the rational design and construction of a novel dual-spatially-confined catalyst of nitrogen-doped carbon (NC) framework encapsulated-amorphous $LaCoO_x$ modified Co nanoparticles embedded in the channel of 2D ordered mesoporous silica (SBA-15(2D)) ($LaCoO_x/Co@NC/SBA-15(2D)$) for efficient ammonia decomposition reaction. It is synthesized by the confined pyrolysis of nano-sized La^{3+} doped ZIF-67 that was in situ grown in the pore channels of SBA-15 under an inert gas atmosphere. Benefiting from the unique structure and composition, the $LaCoO_x/Co@NC/SBA-15$ exhibits enhanced catalytic performance toward NH_3 ammonia decomposition reaction. First, the in situ formed amorphous $LaCoO_x$ species on the surface of Co nanoparticles greatly enhances the adsorption of NH_3 while the

electron-rich Co^0 species promote the activation of NH_3 and recombinative desorption of surface-bound N atoms. Then, the NC matrix can effectively prevent the Co nanoparticles, whether loaded on inside or outside of the pore channels, from agglomeration to enhance the catalytic stability as well as alter the electronic structure of Co nanoparticles to improve the catalytic activity. Finally, the SBA-15(2D) can not only avoid Co nanoparticles sintering at high temperatures via confinement effect, but also improve the accessibility of active sites and mass transfer efficiency. As a result, $LaCoO_x/Co@NC/SBA-15$ exhibits excellent NH_3 decomposition activity, achieving a 100 % ammonia decomposition at 550 °C with a GHSV of 30000 g_{cat}^{-1} h^{-1}. At the same time, it also possesses outstanding high temperature stability, under the harsh conditions of 600 °C and GHSV of 60000 g_{cat}^{-1} h^{-1}, with no change in ammonia decomposition activity after 200 h test and maintains a high H_2 yield of approximately 446 mmol g_{Co}^{-1} min^{-1}, exceeding most of the Co-based catalysts reported to date. This work provides an efficient strategy to simultaneously enhance the activity and stability of cobalt-based nanocatalysts for various catalytic applications.

2. Experimental section

2.1. Materials preparation

2.1.1. Preparation of SBA-15(2D) and SBA-15(3D) supports

First, SBA-15/graphene oxide (GO) composite was prepared by using our reported method with slight modification [33]. Briefly, 6 g of Pluronic P123 and 1.35 g of as-obtained GO were together added into a three-necked flask containing 225 g of 2 M HCl aqueous solution with constant stirring and kept stirring for 24 h at 35 ℃. Then, 12.8 g of tetraethyl orthosilicate was slowly dropped into above suspension and stirred for another 24 h at 35 °C. After that, the temperature was raised to 80 °C and aged for 24 h without agitation. Finally, the obtained product of SBA-15/GO composite was collected by filtration, washed with deionized water and ethanol for 6 times, and dried at 60 °C for 12 h in a vacuum oven. After further calcined at 650 °C for 4 h under air atmosphere to remove the P123 template and graphene oxide, the SBA-15(2D) support was achieved. The preparation method of SBA-15 (3D) support is similar to that of SBA-15(2D), apart from not adding GO in the synthesis process.

2.1.2. Preparation of $LaCoO_x/Co@NC/SBA-15(2D)$, Co@NC/SBA-15 (2D), Ni@NC/SBA-15(2D), Fe@NC/SBA-15(2D), Ru@NC/SBA-15(2D), $LaCoO_x/Co/SBA-15(2D)$, Co/SBA-15(2D), $LaCoO_x/Co@NC/SBA-15$ (3D), and $LaCoO_x/Co@NC$ catalysts

The $LaCoO_x/Co@NC/SBA-15(2D)$ and Co@NC/SBA-15(2D) catalysts were prepared via a nanocasting strategy. For the preparation of $LaCoO_x/Co@NC/SBA-15(2D)$, 0.3 g of SBA-15(2D) support was added to methanol (25 mL), and the suspension was sonicated for 30 min, accompanied by further stirring for 30 min. Then, 0.04 g of $La(NO_3)_3·6$ H_2O was dissolved into above suspension and stirred for 3 h. 0.542 g of $Co(NO_3)_2·6$ H_2O was subsequently added and continued stirred for another 6 h. At the same time, 0.656 g of 2-methylimidazole was added to 25 mL of methanol and the mixture was stirred for 6 h. Then, mixed the two solution and continuously stirred vigorously for 12 h, and the resulting purple suspension was transferred to a vacuum oven at 60 °C until the water was completely evaporated to dryness. The obtained purple solid was grinded in a mortar to achieve uniform powder then heated up to 650 °C from room temperature at a ramping rate of 10 °C min^{-1} and maintained for 2 h in a nitrogen flow. Then, the nitrogen flow was switched to ammonia flow (25 mL min^{-1}) and kept up another 2 h. The $LaCoO_x/Co@NC/SBA-15(2D)$ catalyst was finally obtained after cooling down to room temperature in nitrogen atmosphere. The procedure for the synthesis of Co@NC/SBA-15(2D) is similar to that of $LaCoO_x/Co@NC/SBA-15(2D)$, except that the $La(NO_3)_3·6$ H_2O was not added. The preparation method of Ni@NC/SBA-15(2D), Fe@NC/SBA-15(2D), and Ru@NC/SBA-15(2D) catalysts are similar to that of

Co@NC/SBA-15(2D), except that 0.542 g of Co(NO$_3$)$_2$·6H$_2$O is replaced by 0.540 g of Ni(NO$_3$)$_2$·6H$_2$O, 0.752 g of Fe(NO$_3$)$_2$·9 H$_2$O, and 0.386 g of RuCl$_3$, respectively. The fabrication of LaCoO$_x$/Co/SBA-15(2D) and Co/SBA-15(2D) catalysts follows a similar procedure to that of LaCoO$_x$/Co@NC/SBA-15(2D) and Co@NC/SBA-15(2D), respectively, except that 2-methylimidazole is not added. The preparation process of LaCoO$_x$/Co@NC is similar to that of LaCoO$_x$/Co@NC/SBA-15(2D), except that SBA-15(2D) support is not added. The preparation procedure of LaCoO$_x$/Co@NC/SBA-15(3D) is similar to that of LaCoO$_x$/Co@NC/SBA-15(2D), except that SBA-15(2D) is replaced by SBA-15(3D).

2.2. Materials characterization

X-ray powder diffraction (XRD) was performed on a PANalytical Empyrean diffractometer with Cu Kalpha1 radiation (λ = 1.54178 Å) in the Bragg angle ranging from 10° to 80°. Scanning transmission electron microscopy (STEM) and transmission electron microscopy (TEM) characterizations were performed on a FEI Tecnai F20 field-emission transmission electron microscope (FE-TEM). Scanning electron microscopy (SEM) characterization was acquired on a Hitachi S4800 microscope. Brunauer–Emmett–Teller (BET) surface area measurements were performed on a Micromeritics ASAP 2020 surface area analyzer. Raman spectra were acquired using a LabRAMHR800 spectrograph (Horiba). The excitation source was a helium–neon laser with a wavelength of 534 nm. X-ray photoelectron spectroscopy (XPS) measurements were performed in a Thermo Scientific ESCALAB Xi$^+$ spectrometer equipped with Al K$_\alpha$ X-ray source. H$_2$ temperature-programmed reduction (H$_2$-TPR) analyses were carried out using Builder PCSA-1000 installation with a thermal conductivity detector (TCD). First, 50 mg of as-prepared catalyst was pre-treated in a high-purity nitrogen atmosphere at 300 °C for 30 min, and then cooled down to room temperature. Subsequently, the pre-processed catalysts were reduced in a mixture gas of 5 % H$_2$/95 %Ar using a temperature programme from 50° to 800°C at a ramping rate of 10 °C·min^{-1}. Temperature-programmed decomposition of NH$_3$ (NH$_3$-TPD) experiment was measured on a AutoChem II 2920 chemisorption instrument with an MKS Circus 3 online mass spectrometer. Before the NH$_3$-TPD analysis, 0.1 g of the catalyst was pre-treated at 600 °C for 30 min and then cooled to room temperature under a He atmosphere with a flow rate of 30 mL min^{-1}. After that, a mixture reaction gas of 10 % NH$_3$/90 %Ar was adsorbed for 50 min at the similar flow rate, followed by pure He purging for 1 h to eliminate the gaseous/physically adsorbed NH$_3$ species. Afterwards, the MS signal for fragment species of $m/z = 17$ was recorded at temperature ranging from 50° to 700°C at a rate of 10 °C·min^{-1} in a He flow. Temperature-programmed decomposition of N$_2$ (N$_2$-TPD) experiment was also performed on a AutoChem II 2920 chemisorption instrument with an MKS Circus 3 online mass spectrometer. Before the N$_2$-TPD analysis, 0.1 g of the catalyst was pre-treated at 600 °C for 30 min and then cooled to room temperature under a He atmosphere with a flow rate of 30 mL min^{-1}. After that, the gas flow was changed to N$_2$ for 50 min at the similar flow rate, followed by pure He purging for 1 h to eliminate the gaseous/physically adsorbed N$_2$ species. Afterwards, the MS signal for fragment species of $m/z = 28$ was recorded at temperature ranging from 30° to 650°C at a rate of ≈ 10 °C·min^{-1} in a He flow. CO pulse chemisorption experiment was performed on a BELCAT II chemisorption instrument with a thermal conductivity detector (TCD). Before the experiment, 50 mg of catalyst was pre-reduced in a 10 % H$_2$/Ar mixture gas with a flow rate of 30 mL min^{-1} at 500 °C for 60 min, followed by flushing with pure He for 50 min. After being cooled to 40 °C, the sample was kept in a He flow until the baseline was stabilized. Subsequently, 1.0 mL pulses of 10.12 % CO/He mixture gas were periodically injected into the reduced sample until the sample was saturated adsorbed by CO. Cobalt metal dispersion was calculated via assuming an adsorption stoichiometry of 1:1 for CO/Co.

2.3. Catalytic activity measurements

Catalytic activity measurements for the catalyst were carried out in a quartz tubular flow reactor, and the inner diameter of the reactor was 6 mm. At a flow rate of 30 mL·min^{-1}, 80 mg of tested catalyst was loaded into the reactor, and heated every 10 °C from 350 to 600 °C under pure NH$_3$ flow, each temperature was maintained for 60 min to ensure that the test reaches a stable state. Effluent gases (N$_2$ and NH$_3$) were analysed by an online gas chromatograph equipped with a thermal conductive detector and a Porapark Q column using H$_2$ as the carrier gas. The long-term stability tests of the catalyst were measured at 600 °C for 200 h using a GHSV of 60000 mL·g$_{cat}^{-1}$·h^{-1}. The apparent activation energy (E_a) for decomposition of NH$_3$ was tested by controlling flow rates and tunning the reaction temperatures. The cobalt mass-normalized hydrogen production rate was calculated according to the flowing equation:

$$R_{H_2} = \frac{3}{2} \bullet \frac{V_{NH_3} \bullet X_{NH_3}}{m_{cat} \bullet V_m}$$

whereV_{NH_3}: total molar flow rate (mL min^{-1}), X_{NH_3}: NH$_3$ conversion based on N$_2$ formation, m_{cat}: mass of catalyst in reactor bed (mg), V_m: standard molar volume (22.4 L mol^{-1}).

3. Results and discussion

3.1. Preparation and structural characterization of LaCoO$_x$/Co@NC/SBA-15(2D) catalyst

3.1.1. Synthesis process

The synthesis process of LaCoO$_x$/Co@NC/SBA-15(2D) is schematically illustrated in Scheme 1. First, the SBA-15/P123 composite was assembled to the surface of graphene oxide (GO) by using P123 as the soft template and tetraethoxysilane (TEOS) as the silicon source followed by calcining in air to remove P123 and GO to obtain two-dimensional SBA-15 (SBA-15(2D)) template. Then, a mixed methanol solution of lanthanum nitrate hexahydrate (La(NO$_3$)$_3$·6H$_2$O) and cobalt nitrate hexahydrate (Co(NO$_3$)$_2$·6H$_2$O) was penetrated into the channal of SBA-15(2D) template by wet impregnation and in situ converted to ZIF-67 in channal via adding a organic ligand of 2-methylimidazole to achieve ZIF-67/SBA-15(2D) composite. After drying the ZIF-67/SBA-15(2D) in a vacuum and pyrolyzing at 650 °C in an nitrogen atmosphere followed by activation by ammonia at 650 °C, the LaCoO$_x$/Co@NC/SBA-15(2D) nanocomposite catalyst was obtained. For comparison, under the same conditions, the Co@NC/SBA-15(2D), Fe@NC/SBA-15(2D), Ni@NC/SBA-15(2D), and Ru@NC/SBA-15(2D) catalysts were synthesized without using (La(NO$_3$)$_3$·6H$_2$O) and the LaCoO$_x$/Co/SBA-15(2D) and Co/SBA-15(2D) catalysts were prepared without using 2-methylimidazole. In addition, the LaCoO$_x$/Co/SBA-15(3D) and LaCoO$_x$/Co@NC catalysts were also prepared. See Experiment section for details on catalyst preparation.

3.1.2. Phase structure, morphology, size, and 2D configuration

The TEM images of SBA-15(2D) template reveals that it has a highly ordered two-dimensional pore structure with pore diameter of ≈ 6 nm (Fig. S1). The small angle XRD (SAXRD) pattern shows the strong diffraction peak of the (211) plane of SBA-15 (Fig. S2), further confirming its ordered mesoporous structure. The XRD patterns of the as-synthesized La/ZIF-67/SBA-15(2D) and ZIF-67/SBA-15(2D) composite precursors show the characteristic peaks associated with ZIF-67 [34]. However, the diffraction peaks at 10° in La/ZIF-67/SBA-15(2D) show a little difference with ZIF-67/SBA-15(2D), suggesting that a part of the Co^{2+} is substituted by La^{3+} in ZIF-67, which are confined in the pore channel of the SBA-15(2D) (Fig. S3). After calcination in N$_2$ atmosphere, the obtained catalysts of LaCoO$_x$/Co@NC/SBA-15(2D) and Co@NC/SBA-15(2D) display the diffraction peaks at 44.2°, 51.5°, and
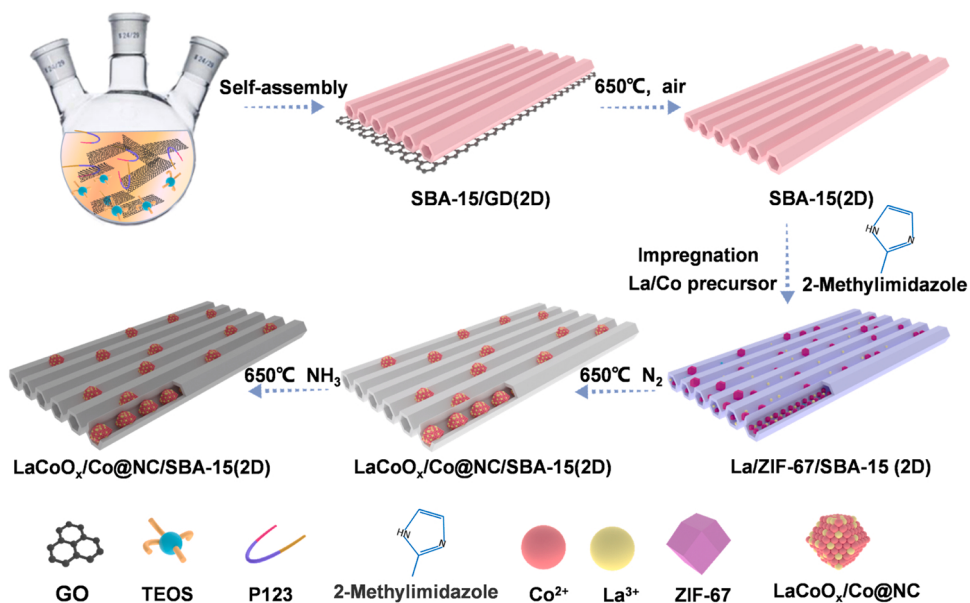
Scheme 1. Schematic illustration of the synthetic procedures of LaCoOx/Co@NC/SBA-15(2D) nanocomposite catalysts.

75.8° assigned to the (111), (200), and (220) planes of β-Co (JCPDS card no.15–0806) along with a broad peak between 15° and 35°(2θ) assigned to amorphous SiO_2 and N doped carbon (NC) framework (Fig. 1a), implying that the ZIF-67 has been converted to

NC-encapsulated Co nanoparticles confined in SBA-15(2D). Meanwhile, the XRD patterns of the $LaCoO_x$/Co/SBA-15(2D) and Co/SBA-15(2D) catalysts prepared by using one-step wet impregnation-reduction method show the same characteristic peaks (Fig. 1a). Notably, no
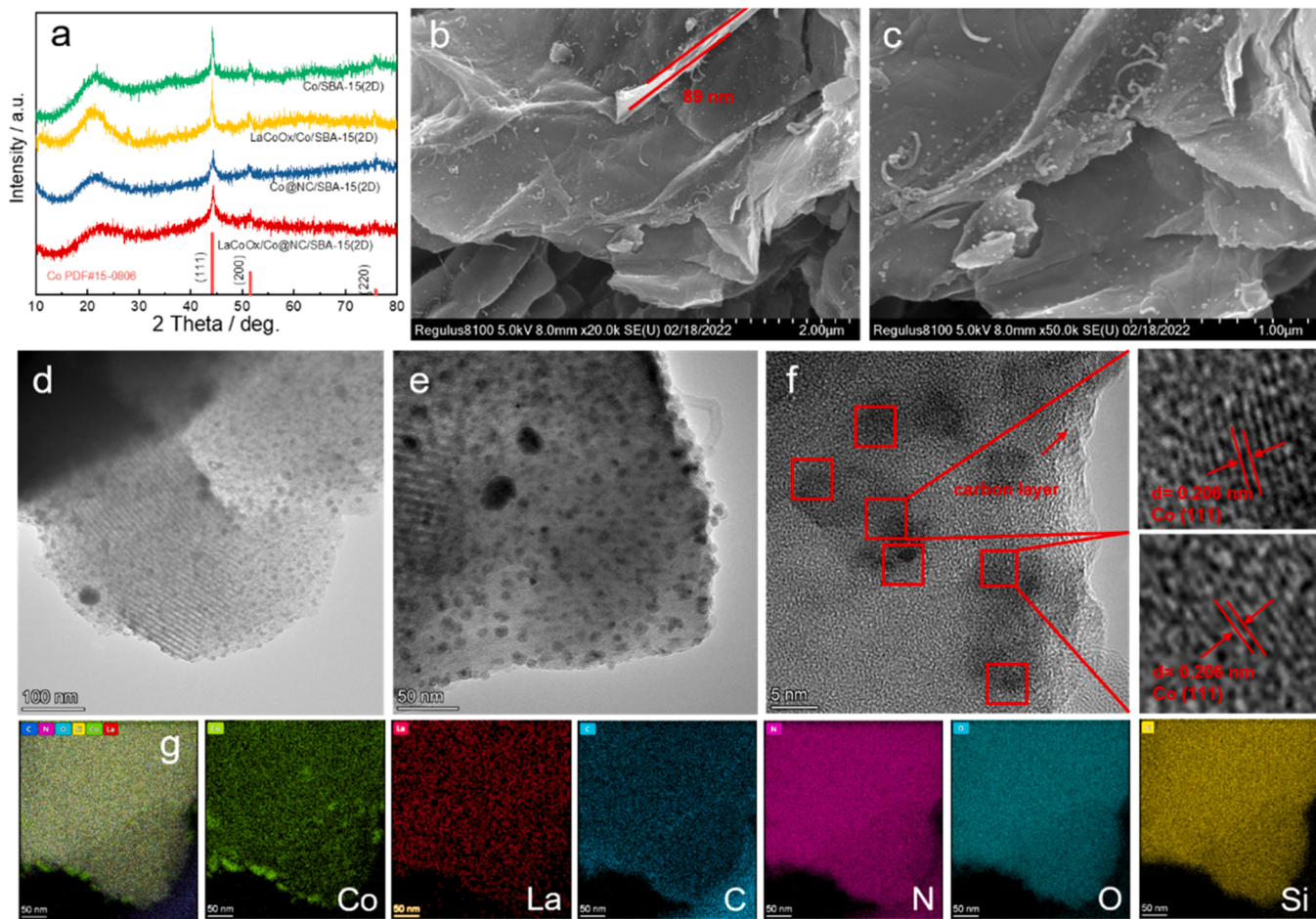

Fig. 1. (a) XRD patterns of $LaCoO_x$/Co@NC/SBA-15(2D) catalysts; (b) and (c) SEM images of $LaCoO_x$/Co@NC/SBA-15(2D); (d), (e) TEM and (f) HRTEM images of $LaCoO_x$/Co@NC/SBA-15(2D); (g) STEM images and corresponding elemental mappings of $LaCoO_x$/Co@NC/SBA-15(2D).

characteristic peaks of LaCoO$_x$ is observed because of the low crystallinity and high dispersion of LaCoO$_x$ in LaCoO$_x$/Co@NC/SBA-15(2D) and LaCoO$_x$/Co/SBA-15(2D) catalysts. In addition, the XRD patterns of the LaCoO$_x$/Co/SBA-15(3D) and LaCoO$_x$/Co@NC catalysts demonstrate that the Co nanoparticles are well crystallized, while the LaCoO$_x$ has a poor crystallinity (Fig. S4).

The SEM images confirm that the LaCoO$_x$/Co@NC/SBA-15(2D) catalyst has a two-dimensional lamellar structure with thickness of about 90 nm (Fig. 1**b**, **c**). The existed the lamellar folds and small-sized nanosheets on the surface of LaCoO$_x$/Co@NC/SBA-15(2D) catalyst should be NC derived from ZIF-67. The SAXRD patterns of the LaCoO$_x$/Co/SBA-15(2D), Co/SBA-15(2D), LaCoO$_x$/Co@/SBA-15(2D), and Co@/SBA-15(2D) catalysts display a characteristic diffraction peak at around 1°, weaker than that of SBA-15(2D) support, indicating that the NC-encapsulated metallic Co and amorphous LaCoO$_x$ nanoparticles are embedded in the pore channels of SBA-15(2D) (Fig. S5). The TEM images show that the LaCoO$_x$/Co@NC/SBA-15(2D) catalyst possesses a highly ordered two-dimensional mesoporous channel structure, the pores are evenly distributed in the two-dimensional direction, in which the ultrafine metallic Co nanoparticles are uniformly embedded in the pore channel of SBA-15(2D) while large-sized ones are loaded on the surface of SBA-15(2D) (Fig. 1**d**, **e**). The HRTEM image displays that the Co nanoparticles show the lattice fringes with a spacing of 0.205 nm, corresponding to the Co(111) crystal plane (Fig. 1**f**). Notably, no lattice fringes associated with graphite carbon around Co nanoparticles can be found, which may be due to the interference of amorphous SiO$_2$ framework. Fortunately, the existed graphite carbon can be verified by their Raman spectra. Clearly, the Raman spectra of the LaCoO$_x$/Co@NC/SBA-15(2D) and Co@NC/SBA-15(2D) catalysts show the characteristic peaks for G band (1347 cm^{-1}) and D band (1590 cm^{-1}) of graphite carbon (Fig. S6), confirming the presence of graphite carbon layer around Co nanoparticles. It is seen that LaCoO$_x$/Co@NC/SBA-15(2D) catalyst shows a higher I$_D$/I$_G$ ratio of 0.99 than that of Co@NC/SBA-15(2D) (0.92), indicating that the LaCoO$_x$/Co@NC/SBA-15(2D) has more disordered carbon and defects, which may endow it more nonmetallic active sites and is conducive to exposing more metallic active sites simultaneously [35,36]. The higher I$_D$/I$_G$ ratio of LaCoO$_x$/Co@NC/SBA-15(2D) may be caused by La^{3+} substituting some Co^{2+} sites in ZIF-67, and these La^{3+} sites will induce the generation of more disordered/defective carbon during pyrolysis, and which can be used as sites for anchoring more small-sized Co nanopartciles and increases the density of active sites [30,37]. In addition, the other two peaks centered at around 475 and 677 cm^{-1} in the Raman spectra of the LaCoO$_x$/Co@NC/SBA-15(2D) Co@NC/SBA-15(2D), LaCoO$_x$/Co/SBA-15(2D), and Co/SBA-15(2D) catalysts can be classified as metallic Co [30,38] (Fig. S6), further suggesting the formation of Co nanoparticles. The EDX elemental mapping images confirm the uniform distribution of Co, La, C, N, O, and Si in the LaCoO$_x$/Co@NC/SBA-15(2D) nanohybrid (Fig. 1**g**), and the existed C and N elements may be related to NC matrix. However, in TEM images of Co@NC/SBA-15(2D), some large nanoparticles are observed, which demonstrates that the presence of amorphous LaCoO$_x$ can effectively inhibit the aggregation of Co nanoparticles (Fig. S7a-**c**). Clearly, the metal nanoparticles evenly distributed in the pore channals of SBA-15(2D) was found in LaCoO$_x$/Co/SBA-15(2D) and Co/SBA-15 (2D) catalysts, confirming that the LaCoO$_x$-modified Co nanoparticles and Co nanoparticles are uniformly confined in SBA-15 (3D) support (Fig. S7d-**i**). For the LaCoO$_x$/Co/SBA-15(3D) catalyst, most of the LaCoO$_x$-modified Co nanoparticles with a uniform size are evenly confined in the pore channels of the SBA-15(3D) support (Fig. S8a-**c**). However, in the LaCoO$_x$/Co@NC catalysts, the irregular LaCoO$_x$-modified Co nanoparticles with an uneven size are embedded in the carbon framework (Fig. S8d-**f**). The content of Co, La, N, Si, O, and C elements in the LaCoO$_x$/Co@NC/SBA-15(2D) catalyst, determined by EDX, was 4.77 at %, 0.08 at %, 2.58 at %, 0.73 at %, 56.71 at %, and 30.11 at %, respectively (Fig. S9), further confirming the existence of NC and LaCoO$_x$ modified Co nanoparticles in SBA-15(2D) support.

3.1.3. Surface area and pore property

The specific surface area and pore structure of the catalysts were probed by nitrogen adsorption/desorption analysis (Fig. S10). The four catalysts of LaCoO$_x$/Co@NC/SBA-15(2D), Co@NC/SBA-15(2D), LaCoO$_x$/Co/SBA-15(2D) and Co/SBA-15(2D) show typical type IV isotherms with an obvious H1 hysteresis loop in the relative pressure (P/P$_0$) from 0.42 to 1.0 [33](Fig. S10a). The Barrett-Joyner-Halenda (BJH) pore size distribution curves verify the existence of mesopores with average pore diameter mainly concentrated at around 3.5 nm in LaCoO$_x$/Co@NC/SBA-15(2D) and Co@NC/SBA-15(2D) while with a bimodal pore distribution at around 3.5 and 4.8 nm in LaCoO$_x$/Co/SBA-15(2D) and Co/SBA-15(2D) (Fig. S10b and Table S1). The specific surface area and pore volume of LaCoO$_x$/Co@NC/SBA-15(2D) are calculated to be 259 m^2·g^{-1} and 0.21 cm^3·g^{-1}, respectively, compared with Co@NC/SBA-15(2D) (277 m^2·g^{-1} and 0.22 cm^3·g^{-1}) (Table S1), indicating that the NC produced by the organic ligands of ZIF-67 after calcination still has the high mesoporous feature. This is favorable for mass and charge transfer during catalytic reactions. The specific surface area of LaCoO$_x$/Co@NC/SBA-15(2D) is slightly lower than that of Co@NC/SBA-15(2D) due to the incorporation of amorphous LaCoO$_x$ in LaCoO$_x$/Co@NC/SBA-15(2D). The surface area of LaCoO$_x$/Co@NC/SBA-15(2D) and Co@NC/SBA-15(2D) catalysts are higher that the corresponding LaCoO$_x$/Co/SBA-15(2D) (205 m^2·g^{-1}) and Co/SBA-15 (2D) (223 m^2·g^{-1}) because the nanopores and defects of NC provides a certain surface area, but the pore volume correspondingly decreases (Table S1), which may be result from the NC framework covering part of the pore channels. The LaCoO$_x$/Co@NC/SBA-15(2D) with larger surface area and more nanopores would provide more catalytic active sites for ammonia decomposition reaction.

3.1.4. Metal dispersion

To verify the full exposure of Co active sites in the prepared catalysts, we carried out the CO pulse chemisorption test for the prepared catalysts to calculate the Co dispersion in different catalysts. Based on CO pulse chemisorption experiment results, it is calculated that the Co dispersion on different catalysts follows the order of LaCoO$_x$/Co@NC/SBA-15(2D) ≈ Co@NC/SBA-15(2D) > LaCoO$_x$/Co/SBA-15(2D) ≈ Co/SBA-15(2D), and the dispersion of Co nanoparticles on LaCoO$_x$/Co@NC/SBA-15 (2D) and Co@NC/SBA-15(2D) catalysts is much higher than that on LaCoO$_x$/Co/SBA-15(2D) and Co/SBA-15(2D) catalysts (Table S2). This result indicates that the coated NC matrix on the surface of LaCoO$_x$/Co and Co can effectively reduce the particle size, promote the dispersion of metallic Co, and allow the full exposure of the active sites, which results in superior activity and stability toward ammonia decomposition reaction.

3.2. NH$_3$ decomposition catalytic performance of LaCoO$_x$/Co@NC/SBA-15(2D) catalyst

The ammonia decomposition performance of the catalyst was tested under a GHSV of 30000 cm^3 g$_{cat}^{-1}$ h^{-1}. In order to investigate the optimal loading of ZIF-67 on SBA-15(2D) support, the catalytic activities of the Co@NC/SBA-15(2D) (1:1), Co@NC/SBA-15(2D) (2:1), and Co@NC/SBA-15(2D) (3:1) catalysts prepared by using different mass ratios of cobalt nitrate hexahydrate and SBA-15(2D) support (1:1, 2:1, and 3:1). Obviously, the Co@NC/SBA-15(2D) (2:1) has the best catalytic activity among these catalysts (Fig. S11). Therefore, the Co-NC/SBA-15(2D) (2:1) catalyst was selected to explore the effect of La^{3+} doping amount (2 wt %, 5 wt %, and 10 wt %) on the catalytic activity of ammonia decomposition (Fig. S12). Among these catalysts, the LaCoO$_x$/Co@NC/SBA-15(2D) with La^{3+} doping amount of 5 wt % possesses the best catalytic activity (Figs. 2**a** and S12). At a GHSV of 30,000 cm^{3}g$_{cat}^{-1}$h^{-1}, for LaCoO$_x$/Co@NC/SBA-15(2D) and Co@NC/SBA-15(2D) catalysts, the NH$_3$ conversion at temperatures between 450 °C and 550 °C are about 35 % higher than those of LaCoO$_x$/Co/SBA-15(2D) and Co/SBA-15(2D) catalysts (Fig. 2**a**). This result may mainly be rooted in two reasons as
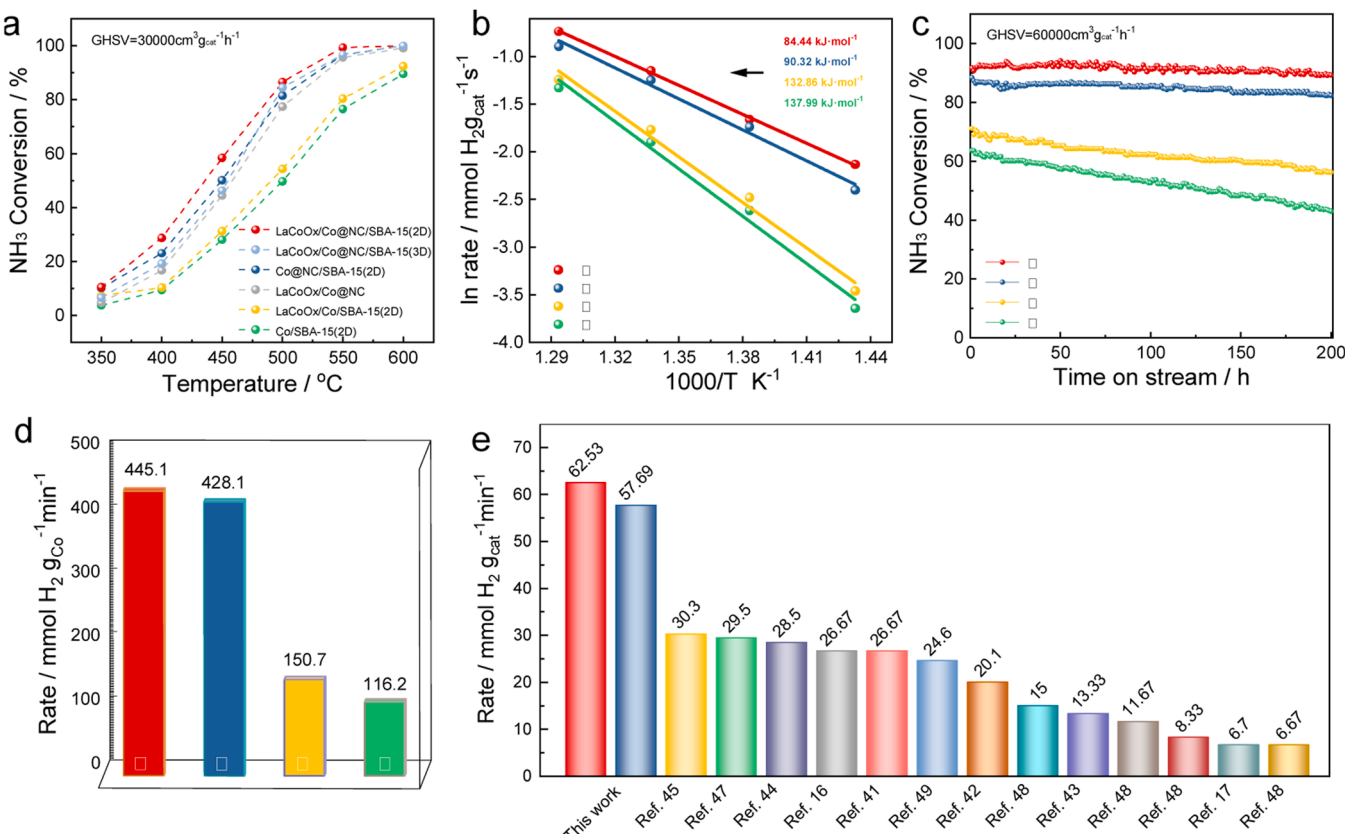
Fig. 2. (a) Temperature dependence of NH$_3$ decomposition activities of different catalysts with a GHSV of 30,000 cm$^3 \cdot$g$_{cat}^{-1} \cdot$h^{-1}; (b) Arrhenius plots; (c) Stability tests under 600 ºC at 60,000 cm$^3 \cdot$g$_{cat}^{-1} \cdot$h^{-1}; (d) hydrogen formation rate of catalysts during the stability test (the data from the end of tests at 200 h), and (e) comparison of the catalytic activity of LaCoO$_x$/Co@NC/SBA-15(2D) and Co@NC/SBA-15(2D) in this work and some reported Co-based and other catalysts at 600 °C. (I) LaCoO$_x$/Co@NC/SBA-15(2D), (II) Co@NC/SBA-15(2D), (III) LaCoO$_x$/Co/SBA-15(2D), and (IV) Co/SBA-15(2D) catalysts.

below. On one hand, the confined effect of NC formwork can refine the grain of Co nanoparticles and increase the number of exposed active sites. On the other hand, the synergistic effect between Co nanoparticles and NC formwork can optimize the electronic structure of Co nanoparticles and enhance the intrinsic activity of Co nanoparticles [37]. The LaCoO$_x$/Co@NC/SBA-15(2D) catalyst reaches a 100 % NH$_3$ conversion at 550 °C, lower than Co@NC/SBA-15(2D) catalyst (600 °C), implying that the LaCoO$_x$, as an effective promoter, can enhance the NH$_3$ decomposition activity of Co nanoparticles because the amorphous short-range ordered LaCoO$_x$ can act as the adsorption sites for moderately bounding N$_2$ molecule and reduces the activation energy of nitrogen desorption [39]. Compared to the LaCoO$_x$/Co@NC/SBA-15(3D) and LaCoO$_x$/Co@NC catalysts, the LaCoO$_x$/Co@NC/SBA-15(2D) catalyst shows a higher ammonia conversion at each temperature, indicating that the SBA-15(2D) support not only avoids Co nanoparticles sintering at high temperatures through the confinement effect, but also improves the accessibility of active sites and mass transfer efficiency (Fig. 2a). Among Co@NC/SBA-15(2D), Ni@NC/SBA-15(2D), Fe@NC/SBA-15 (2D), and Ru@NC/SBA-15(2D) catalysts, the Ru@NC/SBA-15(2D) catalyst shows the best ammonia decomposition activity at temperatures below ~575 °C, while the ammonia decomposition activity of the Co@NC/SBA-15(2D) catalyst is only lower than that of Ru@NC/SBA-15 (2D) catalyst, but better than that of Ni@NC/SBA-15(2D) and Fe@NC/SBA-15(2D) catalysts (Fig. S13 and Table S3). Impressively, the NH$_3$ conversion of Co@NC/SBA-15(2D) catalyst even exceeds that of Ru@NC/SBA-15(2D) catalyst at temperatures above ~575 °C, and the H$_2$ yield follows the order of Co@NC/SBA-15(2D) (33.48 mmol g$_{cat.}^{-1}$ min^{-1}) > Ru@NC/SBA-15(2D) (32.74 mmol g$_{cat.}^{-1}$ min^{-1}) > Ni@NC/SBA-15(2D) (28.63 mmol g$_{cat.}^{-1}$ min^{-1}) > Fe@NC/SBA-15(2D) (25.71 mmol g$_{cat.}^{-1}$ min^{-1}) at 600 °C (Fig. S13 and Table S3). These results

highlight the superior ammonia decomposition activity of the Co@NC/SBA-15(2D) catalyst. The catalytic activity of the SBA-15(2D) support in the temperature range of 350 – 650 °C is negligible, indicating that Co nanoparticles are active species in these catalysts (Fig. S14). The apparent activation energies were calculated using the Arrhenius equation (lnk = lnA – Ea/RT), where k is the rate value and Ea is the apparent activation energy. As shown in Fig. 2b, the LaCoO$_x$/Co@NC/SBA-15(2D) catalyst shows the lowest apparent activation energy of 84.44 kJ mol^{-1}, which is consistent with its NH$_3$ decomposition activity.

Fig. 2c shows the long-term stability test results of LaCoO$_x$/Co@NC/SBA-15(2D), Co@NC/SBA-15(2D), LaCoO$_x$/Co/SBA-15(2D), and Co/SBA-15(2D) catalysts at 600 °C under a high GHSV of 60000 cm^{3}g$_{cat}^{-1}$h^{-1}. Notably, the LaCoO$_x$/Co@NC/SBA-15(2D) and Co@NC/SBA-15(2D) catalysts maintain excellent stability under a harsh condition (Compared with the test of catalytic activity of ammonia decomposition, the NH$_3$ flow rate increases from 40 mL min^{-1} to 80 mL min^{-1}). The LaCoO$_x$/Co@NC/SBA-15(2D) catalyst shows only an approximate 2 % decrease in catalytic activity and still maintains a hydrogen yield of up to 62.53 mmol g$_{cat.}^{-1}$ min^{-1} after a 200 h stability test. Meanwhile, the Co@NC/SBA-15(2D) catalyst can retain a high hydrogen yield of 57.69 mmol g$_{cat.}^{-1}$ min^{-1} at the end of the 200 h test. However, the NH$_3$ decomposition activities of both LaCoO$_x$/Co/SBA-15(2D) and Co/SBA-15(2D) catalysts display obviously deactivation of approximately 21–30 % after a 200 h stability test. The deactivation of activity may be caused by the agglomeration of Co nanoparticles on the catalyst surface, and large-sized and agglomerated Co nanoparticles; this would decrease the number of exposed active sites as well as obstruct a part of the pore channels and decrease mass-transfer efficiency. On the contrary, in the used LaCoO$_x$/Co@NC/SBA-15(2D) and Co@NC/SBA-15(2D) catalysts,

the confined effect of NC matrix can effectively prevent Co nanoparticles on the surface of SBA-15(2D) from further agglomeration. As a result, the LaCoO$_x$/Co@NC/SBA-15(2D) and Co@NC/SBA-15(2D) catalysts exhibit a superior high-temperature stability for ammonia decomposition reaction.

The actual content of Co in different catalysts was measured by ICP-OES to accurately evaluate their NH$_3$ decomposition activities (Table S4). After normalization by the mass of Co in the catalyst, the LaCoO$_x$/Co@NC/SBA-15(2D) catalyst shows a high reaction rate of 445.1 mmol g$_{Co}^{-1}$ min^{-1} at 600 °C, higher than that of Co@NC/SBA-15(2D) (428.1 mmol g$_{Co}^{-1}$ min^{-1}), and about three time as those of LaCoO$_x$/Co@NC/SBA-15(2D) (150.7 mmol g$_{Co}^{-1}$ min^{-1}) and Co@NC/SBA-15(2D) (116.2 mmol g$_{Co}^{-1}$ min^{-1}) catalysts. In fact, such a high H$_2$ generation rate (62.53 mmol g$_{cat.}^{-1}$ min^{-1} or 445.1 mmol g$_{Co}^{-1}$ min^{-1}) also exceeds most of the reported Co-based and other excellent catalysts (Figs. 2e, S13, and Table S5) [16,17,40–49].

The activity of the ammonia decomposition reaction is closely related to the chemical environment and electronic state of the catalyst surface. X-ray photoelectron spectroscopy (XPS) measurements were employed to analyze the elemental composition and valence information of the catalyst surface. The XPS survey spectra (Fig. 3a) show that the existed elements in LaCoO$_x$/Co@NC/SBA-15(2D), Co@NC/SBA-15(2D), LaCoO$_x$/Co/SBA-15(2D), and Co/SBA-15(2D) are consistent with their compositions. As shown in the Fig. 3b, the La 3d XPS spectra can be deconvoluted into two couple peaks, in which the peaks at binding energies of 855.6–855.8 eV and 851.9–852.2 eV correspond to La 3d$_{3/2}$ while the peaks at 838.4–838.9 eV and 835.2–835.4 eV are assigned to La 3d$_{5/2}$. The binding energies of the La 3d peak is consistent with the La-O bonding, and the measured spin-orbit splitting of 16.7 eV is in line with LaCoO$_3$, indicating the formation of LaCoO$_x$ species in the LaCoO$_x$/Co@NC/SBA-15(2D) catalyst [30,32,50]. The O 1s spectra can be deconvoluted into five bands located at binding energies of 529.0–530.1 eV, 530.2–531.6 eV, 531.8–532.3 eV, 532.8–533.2 eV,

and 533.7–533.9 eV (Fig. 3c), corresponding to M-O (M = La or Co) [17], Si-O, surface hydroxyl or oxygen vacancies, C-O bond, and adsorbed water, respectively. The abundant surface hydroxyl groups or oxygen vacancies may be due to the existence of amorphous metal oxidation species with highly coordinated unsaturated metal ions. Therefore, combining the ICP-OES results, EDX elemental mappings, and XPS results, it can be deduced the existence of amorphous LaCoO$_x$ species in LaCoO$_x$/Co@NC/SBA-15(2D) [30]. The Co 2p spectra display two main peaks (Fig. 3d), which belong to the Co 2p$_{3/2}$ and Co 2p$_{1/2}$ orbitals, respectively. The peak in the Co 2p$_{3/2}$ region is divided into three peaks at 780.1–780.5, 782.4–783.1, and 778.1–778.2 eV, which are attributed to Co^{3+}, Co^{2+}, and Co^0 species, respectively [14,31,38,51]. Similarly, in the Co 2p$_{1/2}$ region, the fitted peaks located at binding energies of 795.1–796.3, 796.6–797.1, and 793.2–793.9 eV correspond to Co^{3+}, Co^{2+} and Co^0 species, respectively [38,51,52]. In addition, the two couple broad peaks at 785.8–786.6 eV and 802.7–803.3 eV can be assigned to satellite peaks. The abundant Co^{3+} and Co^{2+} species on the surface of the catalyst may come from the amorphous LaCoO$_x$ species on the surface of Co nanoparticles or the surface oxidation of Co nanoparticles. It is observed that there is no characteristic peak of Co^0 species in Co/SBA-15(2D), which suggests that the superficial Co species exist in the form of oxidation state. The peak intensity of Co^0 species in LaCoO$_x$/Co@NC/SBA-15(2D) is slightly lower than that of Co@NC/SBA-15(2D), which may result from the formation of amorphous LaCoO$_x$ species. In the N 1s XPS spectra (Fig. 3e), the characteristic peaks with binding energies located at 398.6, 400.5 and 401.6 eV are attributable to pyridinic N, pyrrolic N, and graphitic N, respectively [53]. It indicates that the doped nitrogen atoms in carbon matrix derived from the 2-methylimidazole ligand are divided into three types. In the C 1s spectra (Fig. 3f), the fitting peaks at 284.6, 285.5, 286.1, 286.9, and 288.5 eV can be assigned to C–C, C═N, C-O, C═O, and C═C [37,53], further indicating that the N species have been doped in carbon matrix. Meanwhile, the carbon framework has abundant
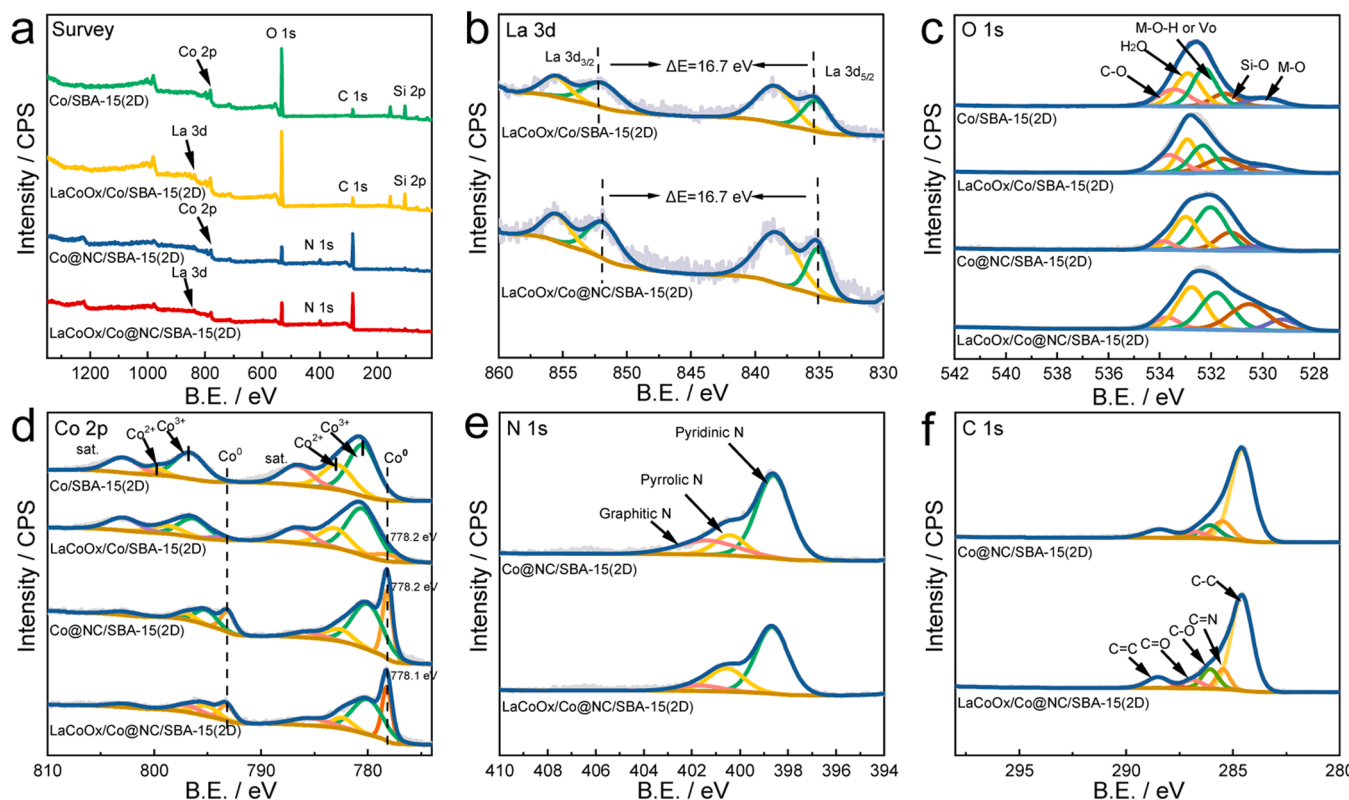
**Fig. 3.** (a) XPS survey spectra of LaCoO$_x$/Co@NC/SBA-15(2D), Co@NC/SBA-15(2D), LaCoO$_x$/Co/SBA-15(2D), and Co/SBA-15(2D) catalysts. High-resolution XPS spectra of LaCoO$_x$/Co@NC/SBA-15(2D), Co@NC/SBA-15(2D), LaCoO$_x$/Co/SBA-15(2D), and Co/SBA-15(2D) for (b) Co, (c) La, (d) C, (e) N and (f) O.

oxygen-containing groups. The nitrogen dopant in the carbon matrix can promote the immobilization of cobalt-containing species [35,38]. Considering the strong interaction between cobalt ions and π electrons [30], cobalt may be preferred to aggregate on sp^2 hybridization nitrogen sites in NC matrix. and realize the in-situ nucleation and tight anchoring of the formed Co nanoparticles. These Co species in the porous NC matrix can serve as the active sites for ammonia decomposition, and resulting in a better catalytic activity [54].

In order to verify the roles of NC and LaCoO$_x$ for promoting the NH$_3$ decomposition activity of the LaCoO$_x$/Co@NC/SBA-15(2D) catalyst. The NH$_3$-TPD and N$_2$-TPD measurements of LaCoO$_x$/Co@NC/SBA-15 (2D), Co@NC/SBA-15(2D), LaCoO$_x$/Co/SBA-15(2D), and Co/SBA-15 (2D) catalysts were performed. The NH$_3$-TPD test is often used to reveal the number and strength of acidic sites for the catalyst, where the adsorption capacity and adsorption ability of the catalyst for NH$_3$ are respectively proportional to the number of the acidic site and the strength of the acidic site, which can be reflected by the desorption peak area and desorption temperature [11,47]. The NH$_3$-TPD profiles show that the area of NH$_3$ desorption peaks for different catalysts follows the order of LaCoO$_x$/Co@NC/SBA-15(2D) > Co@NC/SBA-15(2D) > LaCoO$_x$/Co/SBA-15(2D) ≈ Co/SBA-15(2D) (Fig. 4a), indicating that the composite of NC and LaCoO$_x$ can increase the number of acidic sites for NH$_3$ adsorption and makes the LaCoO$_x$/Co@NC/SBA-15(2D) catalyst has the largest adsorption capacity for NH$_3$. Meanwhile, it is seen that the NH$_3$ desorption peaks for all catalysts are below 300 °C (Fig. 4a), corresponding to the weak acid site, which is commonly regarded as the active site for the NH$_3$ decomposition reaction [11]. The desorption temperature of NH$_3$ on the LaCoO$_x$/Co@NC/SBA-15(2D) catalyst is the highest among these catalysts, reflecting the strongest adsorption ability of weak acid sites for NH$_3$, which is favorable for the adsorption and activation of NH$_3$[11,55]. The NH$_3$ decomposition performance of the

LaCoO$_x$/Co@NC/SBA-15(2D) catalyst can also be reflected by its N$_2$-TPD curve [56]. The N$_2$-TPD profiles show that the desorption peak of N$_2$ on the LaCoO$_x$/Co@NC/SBA-15(2D) surface appears at a lower temperature of ~368 °C compared to that of Co@NC/SBA-15(2D) (~397 °C) (Fig. 4b), implying that the modulation of the active site by LaCoO$_x$ in LaCoO$_x$/Co@NC/SBA-15(2D) catalyst results in a weak strength Co-N bonding energy, which benefits for the recombinative desorption of the bonded N atoms from the catalyst [57,58]. However, the N$_2$ desorption peaks of LaCoO$_x$/Co/SBA-15(2D) and Co/SBA-15(2D) catalysts are located at temperatures of ~419 and ~442 °C, respectively, which are higher than that of Co@NC/SBA-15(2D) and LaCoO$_x$/Co@NC/SBA-15(2D), suggesting a strong strength of Co–N bond. This is not conducive to the recombination and desorption of N atoms to release gas nitrogen from the catalyst surface, thus resulting in a decreased catalytic activity [12,58]. Combining the NH$_3$-TPD and N$_2$-TPD results, it can be deduced that the LaCoO$_x$/Co@NC/SBA-15(2D) catalyst not only facilitates the adsorption and activation of NH$_3$, but also promotes the recombinative desorption of surface-bound N atoms, thereby showing an enhanced NH$_3$ decomposition activity.

The metal-support interaction in the catalyst and its surface reduction effect has large influence on its catalytic activity. Therefore, the H$_2$-TPR was used to analyze the surface reduction behavior of LaCoO$_x$/Co@NC/SBA-15(2D), Co@NC/SBA-15(2D), LaCoO$_x$/Co/SBA-15(2D), and Co/SBA-15(2D) catalysts. The H$_2$-TPR curves show that a pair of reduction peaks at near 380 – 410 °C for the LaCoO$_x$/Co/SBA-15(2D) and Co/SBA-15(2D) catalysts can be observed (Fig. 4c), which should be assigned to the reduction process of Co^{3+} to Co^{2+} and Co^{2+} to Co^0, respectively [59]. In addition, a broad peak at higher temperatures (started at ca. 520 °C) can also be found, which may be ascribed to the reduction of unreduced Co species strongly interacted with the support to metallic Co [11]. However, no reduction peaks (Co^{3+} to Co^{2+} and
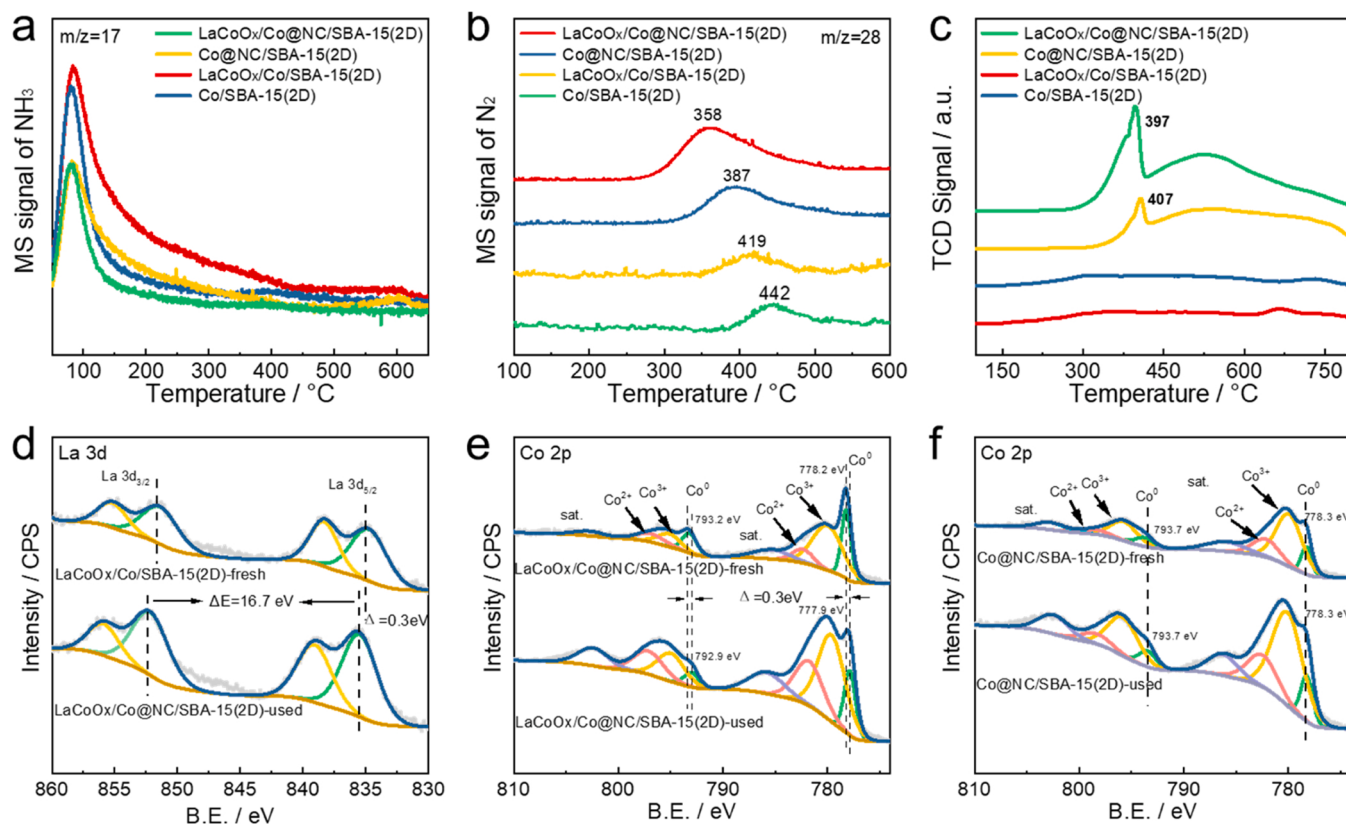

Fig. 4. (a) NH$_3$-TPD, (b) N$_2$-TPD and (c) H$_2$-TPR profiles of LaCoO$_x$/Co@NC/SBA-15(2D), Co@NC/SBA-15(2D), LaCoO$_x$/Co/SBA-15(2D), and Co/SBA-15(2D) catalysts. (d) La 3d and (e) Co 2p spectra of the fresh and used LaCoO$_x$/Co@NC/SBA-15(2D) catalyst. (f) Co 2p spectra of the fresh and used Co@NC/SBA-15 (2D) catalyst.

Co^{2+} to Co^0) were observed at this temperature range in LaCoO$_x$/-Co@NC/SBA-15(2D) and Co@NC/SBA-15(2D) catalysts, implying that the Co species exist in the form of metallic Co nanoparticles, which is consistent with the XPS, XRD, and TEM results (Fig. 3c and Fig. 1a and f). By comparison, it can be deduced that the porous NC matrix can protect the Co species from oxidation. In addition, the broad peak near 660 – 730 °C should correspond to the species that are difficult to be reduced, which may be the high-valance Co species that is incorporated in the skeleton of SBA-15(2D) support via chemical bond or tightly encapsulated by the NC layer [39,57,60]. The above results show that the NC matrix and SBA-15(2D) support can simultaneously stabilize Co nanoparticles, thereby achieving more stable high-temperature catalytic activity.

In order to verify the effect of amorphous LaCoO$_x$ on the catalytic activity of LaCoO$_x$/Co@NC/SBA-15(2D) catalyst, the XPS characterizations were performed on LaCoO$_x$/Co@NC/SBA-15(2D) and Co@NC/SBA-15(2D) before and after reaction. In the Co 2p spectra for the used LaCoO$_x$/Co@NC/SBA-15(2D), the binding energy of Co^0 shifts to a lower direction by ~0.3 eV, suggesting that the LaCoO$_x$ in LaCoO$_x$/Co@NC/SBA-15(2D) can function as an electron donor to provide electrons to Co^0 during the reaction (Fig. 4e). For Co@NC/SBA-15(2D), the surface electronic state of Co^0 has no change significantly after the reaction (Fig. 4f). In the La 3d spectra (Fig. 4d), the binding energy of the La 3d orbital shifts to a higher direction after the reaction in LaCoO$_x$/Co@NC/SBA-15(2D) catalyst. This result further implies the electron

transfer from LaCoO$_x$ species to Co nanoparticles. The electron-rich Co nanoparticles, as active sites, facilitate the successive N-H bond cleavage reactions, the formation of molecular N$_2$ and the subsequently release from the catalyst surface. Therefore, the LaCoO$_x$/Co@NC/SBA-15(2D) catalyst exhibits an enhanced catalytic activity toward NH$_3$ decomposition reaction.

3.3. Structural and textural stability of LaCoO$_x$/Co@NC/SBA-15(2D) catalyst

In ammonia decomposition reaction, the structural and textural stability are of great significance for the catalyst to maintain good long-term catalytic performance. Therefore, we studied the crystalline phase, structure, composite, and surface electronic state of the used LaCoO$_x$/Co@NC/SBA-15(2D), Co@NC/SBA-15(2D), LaCoO$_x$/Co/SBA-15(2D), and Co/SBA-15(2D) after long-term stability test. The XRD results (Fig. 5a) indicate that the catalysts still maintain the metallic phase of β-Co after the ammonia decomposition reaction. In addition, the N$_2$ adsorption-desorption isotherm curves proves that the used catalysts still maintain the mesoporous structure (Fig. 5b, c) with an average pore diameter of 3.4 nm for used LaCoO$_x$/Co@NC/SBA-15(2D) and Co@NC/SBA-15(2D) while a bimodal pore distribution at around 3.5 and 4.8 nm for the used LaCoO$_x$/Co/SBA-15(2D) and Co/SBA-15(2D). Among these used catalysts, the used LaCoO$_x$/Co@NC/SBA-15(2D) catalyst exhibits the highest specific surface area and pore volume of 208 m^2·g^{-1} and
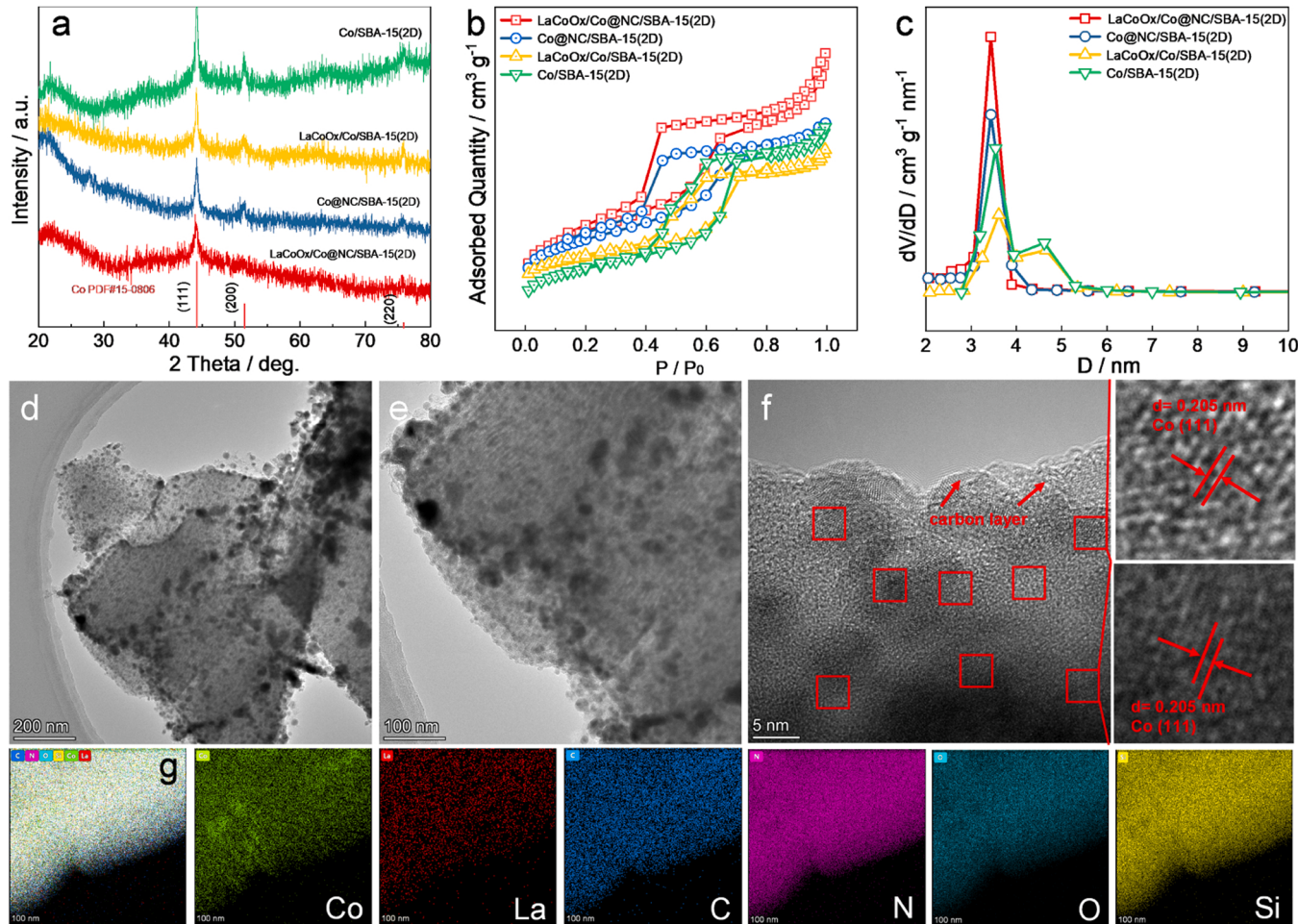
Fig. 5. (a) XRD patterns of the used LaCoO$_x$/Co@NC/SBA-15(2D), Co@NC/SBA-15(2D), LaCoO$_x$/Co/SBA-15(2D, and Co/SBA-15(2D) catalysts. (b) N$_2$ adsorption/desorption isotherms and (c) the corresponding pore size distribution curves of the used LaCoO$_x$/Co@NC/SBA-15(2D), Co@NC/SBA-15(2D), LaCoO$_x$/Co/SBA-15(2D), and Co/SBA-15(2D) catalysts. (d and e) TEM and (f) HRTEM images of the used LaCoO$_x$/Co@NC/SBA-15(2D); (g) STEM images and corresponding elemental mappings of the used LaCoO$_x$/Co@NC/SBA-15(2D).

0.21 m$^2 \cdot$g^{-1}, far higher than those of used LaCoO$_x$/Co/SBA- 15(2D) (88 m$^2 \cdot$g^{-1} and 0.13 cm$^3 \cdot$g^{-1}) and Co/SBA-15(2D) (116 m$^2 \cdot$g^{-1} and 0.17 cm$^3 \cdot$g^{-1}) catalysts, slightly higher than that of Co@NC/SBA-15(2D) catalyst (188 m$^2 \cdot$g^{-1} and 0.18 cm$^3 \cdot$g^{-1}) (Table S1). Clearly, compared to the fresh catalysts, the decrease degree of specific surface area of the used LaCoO$_x$/Co/SBA-15(2D) and Co/SBA-15(2D) catalysts are obviously larger than those of the used LaCoO$_x$/Co@NC/SBA-15(2D) and Co@NC/SBA-15(2D) catalysts, which may be due to partial agglomerated Co nanoparticles block the mesoporous pore channels and reduce the number of exposed active sites. This result confirms that the NC matrix can effectively prevent the Co nanoparticles from sintering and maintain the number of exposed active sites as well as provides a fluent mass-transfer channel for the catalyst at high temperatures. In addition, the drop of specific surface area for the used LaCoO$_x$/Co@NC/SBA-15 (2D) is lower than that of the used Co@NC/SBA-15(2D), implying that the incorporation of LaCoO$_x$ can effectively prevent the Co nanoparticles from sintering during high-temperature reaction. The higher surface area and pore volume of LaCoO$_x$/Co@NC/SBA-15(2D) provides a guarantee for the catalyst to easily access to NH$_3$. In the TEM images (Fig. 5d, e and Fig. S15), it can be observed that the structure of the used LaCoO$_x$/Co@NC/SBA-15(2D) and Co@NC/SBA-15(2D) catalysts is maintained well, and the two-dimensional channels can be clearly seen. Meanwhile, most of the Co nanoparticles are still embedded in the pore channels of SBA-15, and the Co nanoparticles loaded on the outside of pore channel have no significant reunion. The HRTEM image shows that Co nanoparticles display the lattice fringes with an interplanar distance of 0.205 nm, corresponding to the Co (111) crystal plane (Fig. 5f). The EDX mapping images still confirm the uniform distribution of Co, La, C, N, O, and Si in the LaCoO$_x$/Co@NC/SBA-15(2D) nanohybrid (Fig. 5g). For other used catalysts of LaCoO$_x$/Co/SBA-15(2D) and Co/SBA-15(2D), large-sized nanoparticles can be found in their TEM images (Fig. S15), suggesting that the Co nanoparticles loaded on the surface of SBA-15 (2D) occur obvious agglomeration at high temperature. This indicates that the confined of NC framework can indeed enhance the stability of Co nanoparticles. In the La 3d spectra (Fig. S16b), the spin-orbit splitting energy of La3d$_{5/2}$ and La3d$_{3/2}$ is still 16.7 eV, which is consistent with LaCoO$_3$ (16.7 eV), implying that the La species still presents in the form of LaCoO$_x$. Notably, in the O 1 s spectra (Fig. S16c), the intensity of M-O in the used LaCoO$_x$/Co@NC/SBA-15(2D) is higher than that of the used Co@NC/SBA-15(2D) because the LaCoO$_x$ contains more M-O species. In the Co 2p XPS spectra (Fig. S16d), the increased peak intensity for Co^0 is found in the used LaCoO$_x$/Co/SBA-15(2D) and Co/SBA-15(2D) catalysts in comparison with the fresh ones (Fig. 3c) because a portion of Co species with high-valence is reduced in the reduction atmosphere of NH$_3$. Pyridinic N, pyrrolic N, and graphitic N species were still observed in the N 1 s spectra of the used LaCoO$_x$/Co@NC/SBA-15(2D) and Co@NC/SBA-15(2D) catalysts (Fig. S16e). Meanwhile, in their C 1 s spectra, the characteristic peaks at 284.6, 285.5, 286.2, 286.9, and 288.5 eV, attributable to C–C, C=N, C–O, C=O, and C=C, were also observed (Fig. S16f). Both results show that the NC matrix still exists.

3.4. Theoretical consideration

To gain further insight of enhanced ammonia decomposition properties, the spin polarized density functional theory (DFT) calculations were performed to investigate the pathways of NH$_3$ decomposition on Co (111) and LaCoO$_3$/Co (111) (Fig. S17). In general, the mechanism of NH$_3$ decomposition reaction on the catalyst surface can be realized by cleavage of the N-H bonds and recombinative desorption of N$_2$ as follows:

$$NH_3 + * \rightarrow NH_{3,ad} \tag{1}$$

$$NH_{3,ad} + * \rightarrow NH_{2,ad} + H* \tag{2}$$

$$NH_{2,ad}* + * \rightarrow NH_{ad} + H* \tag{3}$$

$$NH_{ad}* + * \rightarrow N_{ad} + H* \tag{4}$$

$$H* + H* \rightarrow H_2 + 2* \tag{5}$$

$$N_{ad} + N_{ad} \rightarrow N_2 + 2* \tag{6}$$
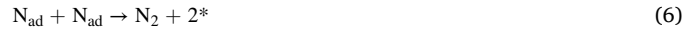
where the asterisk (*) and NH$_{x,ad}$ (x = 0–3) denote the vacant sites and intermediate species adsorbed on the catalyst surface, respectively. The reaction routes of NH$_3$ dissociation and N$_2$ desorption are first studied step by step on Co (111) and LaCoO$_3$/Co(111) surfaces. The corresponding energy profiles with the most stable structures of the intermediates in NH$_3$ decomposition reaction, the calculated adsorption energies (E_{abs}) of the corresponding intermediates, the energy barriers (E_a) and the reaction energies (ΔE_r) on two catalyst surfaces are shown in Fig. 6 and Table S6. Meanwhile, the *d* electron configuration of Co (111) and LaCoO$_3$/Co(111) and charge density difference in LaCoO$_3$/Co (111) are also calculated and displayed in Fig. S18. Clearly, the adsorption energies of NH$_2$, NH, N, and H species on LaCoO$_3$/Co(111) are more negative than those on Co(111), implying that these species are more favorable to adsorption to the LaCoO$_3$/Co(111) surface (Fig. 6a). For the whole dehydrogenation progress of NH$_x$ on Co(111) and LaCoO$_3$/Co(111), all the adsorption processes of NH$_x$ species on two surfaces are exothermic, and four reaction energies on Co(111) are 0.70, −0.92, 0.09, and 1.02 eV, respectively while the corresponding reaction energies on LaCoO$_3$/Co(111) are −0.50, −0.36, 0.68, and 0.71 eV, respectively (Table S6). Clearly, the elementary reaction of H* + H*→ H$_2$ + 2* on Co(111) and LaCoO$_3$/Co(111) has the highest positive reaction energy, and the reaction energy on Co(111) is more positive than that on LaCoO$_3$/Co(111) (1.02 eV vs. 0.71 eV). This result indicates the dehydrogenation of NH$_3$ is more thermodynamically favorable on the LaCoO$_3$/Co(111) surface. Furthermore, most of the previous studies have revealed that the desorption of nitrogen is a good descriptor for identifying whether the catalyst has a promising catalytic activity [33, 61], thereby the pathways of N$_2$ desorption were calculated. As shown in Fig. 6b, the energy barriers of nitrogen formation on Co(111) and LaCoO$_3$/Co(111) are 2.00 and 1.59 eV with the reaction energies of 0.85 and 0.58 eV, respectively (Table S7). In view of this consequence, the nitrogen formation energy barrier is largest in the entire catalytic process of NH$_3$ decomposition and the recombinative desorption of bonded N atom is the rate-determining step. Furthermore, the lower energy barrier for the correlative desorption of bonded N atoms on LaCoO$_3$/Co (111) than that on Co(111) means that corresponding desorption of N atoms on LaCoO$_3$/Co(111) is more easily, which is beneficial to recovery and exposure of the active sites, and results in an enhanced ammonia decomposition activity.

Previous studies have demonstrated that a *d*-band center closer to the Fermi level might lead to a strengthen interaction between reactent and catalyst [58,59]. The calculated *d*-band center of LaCoO$_3$/Co(111) is closer to zero than that of Co(111) (−1.09 vs. −1.18 eV), and the adsorption energy for the adsorbed NH$_3$ specie on LaCoO$_3$/Co(111) is higher than that on Co (111) (−1.08 vs. −0.76 eV (Fig. S18a and Fig. 6a), which is consistent with the conclusion that the adsorption energy is related to the *d*-band center [62]. Furthermore, the analysis of charge density differences (Fig. S18b) displays obvious electron transfer between LaCoO$_3$ and Co in LaCoO$_3$/Co(111), which benefits for generating plenty of active sites for NH$_3$ adsorption in LaCoO$_3$/Co(111). To gain further in-depth understanding of the enhancement of NC matrix on the activity, the N$_2$ desorption pathways on Co(111)/NC and LaCoO$_3$/Co (111)/NC were also calculated (Fig. 6c). Obviously, the N$_2$ formation energy barriers on LaCoO$_3$/Co(111)/NC and Co (111)/NC composites are calculated to be 1.52 and 1.73 eV, respectively, lower than that on LaCoO$_3$/Co(111) (1.59 eV) and Co(111) (2.00 eV) surfaces. This result reveals that the introduction of NC matrix can effectively weaken the associative desorption of adsorbed N atoms and thus improve NH$_3$ decomposition activity, well matching with the experimental results (Fig. 3a).
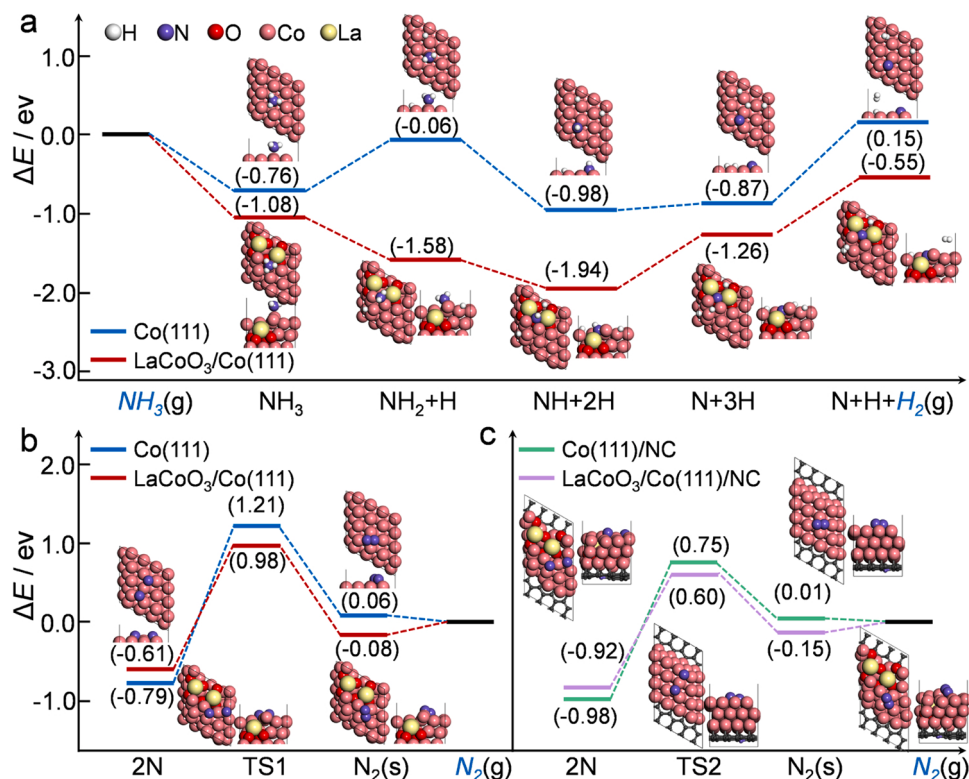
Fig. 6. The energy profiles of NH₃ decomposition reaction: (a) the stepwise dehydrogenation processes of NH$_x$, (b) the associative desorption of nitrogen atoms on Co (111) and LaCoO₃/Co(111), and (c) the associative desorption of nitrogen atoms on Co(111)/NC and LaCoO₃/Co(111)/NC. TS represents the transition state. The Co, La, N, O, and H atoms are marked in pink, yellow, violet, red and white.

4. Conclusion

In conclusion, we report the synthesis of two-dimensional SBA-15 and N doped carbon framework dual confined amorphous LaCoO$_x$-modified Co nanoparticles (LaCoO$_x$/Co@NC/SBA-15(2D)) as a highly active and stable catalyst for efficient ammonia decomposition reaction. It shows an outstanding NH₃ decomposition performance and can achieve a 100 % ammonia decomposition at 550 °C with a GHSV of 30000 g$_{cat}^{-1}$ h^{-1}, superior to that of Co@NC/SBA-15(2D), LaCoO$_x$/Co/ SBA-15(2D), and Co/SBA-15(2D). Meanwhile, it maintains a high H₂ yield of approximately 446 mmol g$_{Co}^{-1}$ min^{-1} under the harsh conditions of 600 °C and GHSV of 60000 g$_{cat}^{-1}$ h^{-1} for 200 h, surpassing most of Co-based catalysts reported so far. Various characterizations and theoretical calculations results verify that the outstanding NH₃ decomposition performance of LaCoO$_x$/Co@NC/SBA-15(2D) catalyst may mainly root in several reasons as below: (i) the amorphous LaCoO$_x$ species greatly enhances the adsorption of NH₃; (ii) the electron-rich Co^0 nanoparticles promotes the activation of NH₃ and the recombination desorption of surface-bound N atoms; (iii) the encapsulated N-doped carbon framework can effectively prevent the Co nanoparticles, whether loaded on inside or outside of the pore channels, from agglomeration to enhance the catalytic stability as well as alter the electronic structure of Co nanoparticles to weaken the associative desorption of adsorbed N atoms and thus improve the catalytic activity; (iv) the SBA-15(2D) not only avoids Co nanoparticles sintering at high temperatures through confinement effects, but also improves the accessibility of active sites and mass transfer efficiency. This versatile dual-space confinement strategy effectively improves the high-temperature durability and mechanical strength of the materials, which can be extended to the fabrication of other 2D porous substance confined metal nanoparticles catalyst/electrode for various promising energy storage and conversion applications.

CRediT authorship contribution statement

Xi Han carried out experiments and wrote the original manuscript; **Minghao Hu** and **Rui Gao** carried out the DFT calculations and wrote the section of theoretical consideration; **Junchao Yu** added the experimental data and analysis; **Baocang Liu** and **Jun Zhang** conceived the idea, designed the research, and guided experiments and data analysis. **Baocang Liu**, **Xuan Xu**, and **Peng Jing** revised the manuscript. All authors contributed to interpreting the results and revising the manuscript.

Declaration of Competing Interest

The authors declare that they have no known competing financial interests or personal relationships that could have appeared to influence the work reported in this paper.

Data availability

The authors do not have permission to share data.

Leading Talent" Program of Inner Mongolia, the "Grassland Talent" Innovation Team of Inner Mongolia, the "Science and Technology for a Better Development of Inner Mongolia" Program (2020XM03), and the Science and Technology Project of Ordos (2021 ZDI 11-14).

Appendix A. Supporting information

Supplementary data associated with this article can be found in the online version at doi:10.1016/j.apcatb.2023.122534.

References

[1] T. John A, Sustainable hydrogen production, Science 305 (2004) 972–974, https:// doi.org/10.1126/science.1103197.

[2] I. Lucentini, X. Garcia, X. Vendrell, J. Llorca, Review of the decomposition of ammonia to generate hydrogen, Ind. Eng. Chem. Res. 60 (2021) 18560–18611, https://doi.org/10.1021/acs.iecr.1c00843.

[3] N. Armaroli, V. Balzani, The future of energy supply: challenges and opportunities, Angew. Chem. Int. Ed. 46 (2007) 52–66, https://doi.org/10.1002/ anie.200602373.

[4] F. Schüth, R. Palkovits, R. Schlögl, D.S. Su, Ammonia as a possible element in an energy infrastructure: catalysts for ammonia decomposition, Energy Environ. Sci. 5 (2012) 6278–6289, https://doi.org/10.1039/c2ee02865d.

[5] S. Mukherjee, S.V. Devaguptapu, A. Sviripa, C.R.F. Lund, G. Wu, Low-temperature ammonia decomposition catalysts for hydrogen generation, Appl. Catal., B 226 (2018) 162–181, https://doi.org/10.1016/j.apcatb.2017.12.039.

[6] X.-C. Hu, X.-P. Fu, W.-W. Wang, X. Wang, K. Wu, R. Si, C. Ma, C.-J. Jia, C.-H. Yan, Ceria-supported ruthenium clusters transforming from isolated single atoms for hydrogen production via decomposition of ammonia, Appl. Catal., B 268 (2020), 118424, https://doi.org/10.1016/j.apcatb.2019.118424.

[7] H.B. Kim, E.D. Park, Ammonia decomposition over Ru catalysts supported on alumina with different crystalline phases, Catal. Today (2022), https://doi.org/ 10.1016/j.cattod.2022.06.032.

[8] J. Cha, T. Lee, Y.-J. Lee, H. Jeong, Y.S. Jo, Y. Kim, S.W. Nam, J. Han, K.B. Lee, C. W. Yoon, H. Sohn, Highly monodisperse sub-nanometer and nanometer Ru particles confined in alkali-exchanged zeolite Y for ammonia decomposition, Appl. Catal., B 283 (2021), 119627, https://doi.org/10.1016/j.apcatb.2020.119627.

[9] P.F. Ng, Li, S. Wang, Z. Zhu, G. Lu, Z. Yan, Catalytic ammonia decomposition over industrial-waste-supported Ru catalysts, Environ. Sci. Technol. 41 (2007) 3758–3762, https://doi.org/10.1021/es062326z.

[10] T.A. Le, Y. Kim, H.W. Kim, S.-U. Lee, J.-R. Kim, T.-W. Kim, Y.-J. Lee, H.-J. Chae, Ru-supported lanthania-ceria composite as an efficient catalyst for CO$_x$-free H$_2$ production from ammonia decomposition, Appl. Catal., B 285 (2021), 119831, https://doi.org/10.1016/j.apcatb.2020.119831.

[11] X.-C. Hu, W.-W. Wang, Z. Jin, X. Wang, R. Si, C.-J. Jia, Transition metal nanoparticles supported La-promoted MgO as catalysts for hydrogen production via catalytic decomposition of ammonia, J. Energy Chem. 38 (2019) 41–49, https://doi.org/10.1016/j.jechem.2018.12.024.

[12] L. Wang, Y. Yi, Y. Zhao, R. Zhang, J. Zhang, H. Guo, NH$_3$ decomposition for H$_2$ generation: effects of cheap metals and supports on plasma–catalyst synergy, ACS Catal. 5 (2015) 4167–4174, https://doi.org/10.1021/acscatal.5b00728.

[13] Z. Lendzion-Bielun, U. Narkiewicz, W. Arabczyk, Cobalt-based catalysts for ammonia decomposition, Materials 6 (2013) 2400–2409, https://doi.org/ 10.3390/ma6062400.

[14] L. Li, R. Jiang, W. Chu, H. Cang, H. Chen, J. Yan, Cobalt nanoparticles embedded in a porous carbon matrix as an efficient catalyst for ammonia decomposition, Catal. Sci. Technol. 7 (2017) 1363–1371, https://doi.org/10.1039/c7cy00086c.

[15] D. Varisli, N.G. Kaykac, CO$_x$ free hydrogen production over cobalt incorporated silicate structured mesoporous catalysts, Appl. Catal., B 127 (2012) 389–398, https://doi.org/10.1016/j.apcatb.2012.08.042.

[16] X. Duan, G. Qian, X. Zhou, D. Chen, W. Yuan, MCM-41 supported Co Mo bimetallic catalysts for enhanced hydrogen production by ammonia decomposition, Chem. Eng. J. 207–208 (2012) 103–108, https://doi.org/10.1016/j.cej.2012.05.100.

[17] C. Huang, Y. Yu, X. Tang, Z. Liu, J. Zhang, C. Ye, Y. Ye, R. Zhang, Hydrogen generation by ammonia decomposition over Co/CeO$_2$ catalyst: influence of support morphologies, Appl. Surf. Sci. 532 (2020), 147335, https://doi.org/10.1016/j. apsusc.2020.147335.

[18] M. Zybert, A. Tarka, B. Mierzwa, L. Kępiński, W. Raróg-Pilecka, Promotion effect of lanthanum on the Co/La/Ba ammonia synthesis catalysts—the influence of lanthanum content, Appl. Catal., A 515 (2016) 16–24, https://doi.org/10.1016/j. apcata.2016.01.036.

[19] H. Zhang, Y.A. Alhamed, W. Chu, Z. Ye, A. AlZahrani, L. Petrov, Controlling Co-support interaction in Co/MWCNTs catalysts and catalytic performance for hydrogen production via NH$_3$ decomposition, Appl. Catal., A 464–465 (2013) 156–164, https://doi.org/10.1016/j.apcata.2013.05.046.

[20] H. Liu, H. Wang, J. Shen, Y. Sun, Z. Liu, Promotion effect of cerium and lanthanum oxides on Ni/SBA-15 catalyst for ammonia decomposition, Catal. Today 131 (2008) 444–449, https://doi.org/10.1016/j.cattod.2007.10.048.

[21] L. Liu, X. Yang, Y. Xie, H. Liu, X. Zhou, X. Xiao, Y. Ren, Z. Ma, X. Cheng, Y. Deng, D. Zhao, A universal Lab-on-Salt-particle approach to 2D single-layer ordered mesoporous materials, Adv. Mater. 32 (2020) 1906653, https://doi.org/10.1002/ adma.201906653.

[22] X. Yang, Y. Li, J. Ma, Y. Zou, X. Zhou, X. Cheng, F.A. Alharthi, A.A. Alghamdi, Y. Deng, General and efficient synthesis of two-dimensional monolayer mesoporous materials with diverse framework compositions, ACS Appl. Mater. Interfaces 13 (2021) 1222–1233, https://doi.org/10.1021/acsami.0c18027.

[23] X. Sun, A.I.O. Suarez, M. Meijerink, T. van Deelen, S. Ould-Chikh, J. Zečević, K. P. de Jong, F. Kapteijn, J. Gascon, Manufacture of highly loaded silica-supported cobalt fischer–tropsch catalysts from a metal organic framework, Nat. Commun. 8 (2017) 1680, https://doi.org/10.1038/s41467-017-01910-9.

[24] S. Luo, X. Li, B. Zhang, Z. Luo, M. Luo, Mof-derived Co$_3$O$_4$@NC with core–shell structures for N$_2$ electrochemical reduction under ambient conditions, ACS Appl. Mater. Interfaces 11 (2019) 26891–26897, https://doi.org/10.1021/ acsami.9b07100.

[25] Z. Hu, J. Mahin, L. Torrente-Murciano, A MOF-templated approach for designing ruthenium–cesium catalysts for hydrogen generation from ammonia, Int. J. Hydrogen Energy 44 (2019) 30108–30118, https://doi.org/10.1016/j. ijhydene.2019.09.174.

[26] J. Tang, S. Jiang, Y. Liu, S. Zheng, L. Bai, J. Guo, J. Wang, Electrochemical determination of dopamine and uric acid using a glassy carbon electrode modified with a composite consisting of a Co(ii)-based metalorganic framework (ZIF-67) and graphene oxide, Mikrochim. Acta 185 (2018) 486, https://doi.org/10.1007/ s00604-018-3025-x.

[27] S.J. Wang, S.F. Yin, L. Li, B.Q. Xu, C.F. Ng, C.T. Au, Investigation on modification of Ru/CNTs catalyst for the generation of CO$_x$-free hydrogen from ammonia, Appl. Catal., B 52 (2004) 287–299, https://doi.org/10.1016/j.apcatb.2004.05.002.

[28] S. Bajus, F. Agel, M. Kusche, N. Ní Bhriain, P. Wasserscheid, Alkali hydroxide-modified Ru/γ-Al$_2$O$_3$ catalysts for ammonia decomposition, Appl. Catal., A 510 (2016) 189–195, https://doi.org/10.1016/j.apcata.2015.11.024.

[29] C. Huang, H. Li, J. Yang, C. Wang, F. Hu, X. Wang, Z.-H. Lu, G. Feng, R. Zhang, Ce$_{0.6}$Zr$_{0.3}$Y$_{0.1}$O$_2$ solid solutions-supported Ni Co bimetal nanocatalysts for NH$_3$ decomposition, Appl. Surf. Sci. 478 (2019) 708–716, https://doi.org/10.1016/j. apsusc.2019.01.269.

[30] L. Gao, J. Xie, S. Liu, S. Lou, Z. Wei, X. Zhu, B. Tang, Crystalline cobalt/amorphous LaCoO$_x$ hybrid nanoparticles embedded in porous nitrogen-doped carbon as efficient electrocatalysts for hydrazine-assisted hydrogen production, ACS Appl. Mater. Interfaces 12 (2020) 24701–24709, https://doi.org/10.1021/ acsami.0c02124.

[31] E.V. Makshina, N.S. Nesterenko, S. Siffert, E.A. Zhilinskaya, A. Aboukais, B. V. Romanovsky, Methanol oxidation on laco mixed oxide supported onto MCM-41 molecular sieve, Catal. Today 131 (2008) 427–430, https://doi.org/10.1016/j. cattod.2007.10.088.

[32] X. Wang, X. Peng, H. Ran, B. Lin, J. Ni, J. Lin, L. Jiang, Influence of Ru substitution on the properties of LaCoO$_3$ catalysts for ammonia synthesis: XAFS and XPS studies, Ind. Eng. Chem. Res. 57 (2018) 17375–17383, https://doi.org/10.1021/ acs.iecr.8b04915.

[33] L. Huo, X. Han, L. Zhang, B. Liu, R. Gao, B. Cao, W.-W. Wang, C.-J. Jia, K. Liu, J. Liu, J. Zhang, Spatial confinement and electron transfer moderating Mo-N bond strength for superior ammonia decomposition catalysis, Appl. Catal., B 294 (2021), 120254, https://doi.org/10.1016/j.apcatb.2021.120254.

[34] A.D. Phan, C.J. Uribe-Romo, F.J. Knobler, C.B. O'Keeffe, M. Yaghi, O. M, Synthesis, structure, and carbon dioxide capture properties of zeolitic imidazolate frameworks, Acc. Chem. Res 43 (2010) 58–67, https://doi.org/10.1021/ ar900116g.

[35] Y. Chen, S. Ji, Y. Wang, J. Dong, W. Chen, Z. Li, R. Shen, L. Zheng, Z. Zhuang, D. Wang, Y. Li, Isolated single iron atoms anchored on N-doped porous carbon as an efficient electrocatalyst for the oxygen reduction reaction, Angew. Chem. Int. Ed. 56 (2017) 6937–6941, https://doi.org/10.1002/anie.201702473.

[36] W. Zhang, X. Yao, S. Zhou, X. Li, L. Li, Z. Yu, L. Gu, Zif-8/ZIF-67-derived Co-N$_x$-embedded 1D porous carbon nanofibers with graphitic carbon-encased Co nanoparticles as an efficient bifunctional electrocatalyst, Small 14 (2018), e1800423, https://doi.org/10.1002/smll.201800423.

[37] B. Qiu, C. Yang, W. Guo, Y. Xu, Z. Liang, D. Ma, R. Zou, Highly dispersed Co-based fischer–tropsch synthesis catalysts from metal–organic frameworks, J. Mater. Chem. A 5 (2017) 8081–8086, https://doi.org/10.1039/c7ta02128c.

[38] T. Wang, Z. Kou, S. Mu, J. Liu, D. He, I.S. Amiinu, W. Meng, K. Zhou, Z. Luo, S. Chaemchuen, F. Verpoort, 2D dual-metal zeolitic-imidazolate-framework-(ZIF)-derived bifunctional air electrodes with ultrahigh electrochemical properties for rechargeable zinc-air batteries, Adv. Funct. Mater. 28 (2018), https://doi.org/ 10.1002/adfm.201705048.

[39] P. Xiao, J. Zhu, H. Li, W. Jiang, T. Wang, Y. Zhu, Y. Zhao, J. Li, Effect of textural structure on the catalytic performance of LaCoO$_3$ for Co oxidation, ChemCatChem 6 (2014) 1774–1781, https://doi.org/10.1002/cctc.201402064.

[40] H. Zhang, Y.A. Alhamed, A. Al-Zahrani, M. Daous, H. Inokawa, Y. Kojima, L. A. Petrov, Tuning catalytic performances of cobalt catalysts for clean hydrogen generation via variation of the type of carbon support and catalyst post-treatment temperature, Int. J. Hydrogen Energy 39 (2014) 17573–17582, https://doi.org/ 10.1016/j.ijhydene.2014.07.183.

[41] J. Ji, X. Duan, G. Qian, X. Zhou, G. Tong, W. Yuan, Towards an efficient CoMo/ γ-Al$_2$O$_3$ catalyst using metal amine metallate as an active phase precursor: enhanced hydrogen production by ammonia decomposition, Int. J. Hydrog. Energy 39 (2014) 12490–12498, https://doi.org/10.1016/j.ijhydene.2014.06.081.

[42] Z.-S. Zhang, X.-P. Fu, W.-W. Wang, Z. Jin, Q.-S. Song, C.-J. Jia, Promoted porous Co$_3$O$_4$-Al$_2$O$_3$ catalysts for ammonia decomposition, Sci. China Chem. 61 (2018) 1389–1398, https://doi.org/10.1007/s11426-018-9261-5.

[43] Jian Zhang, Jens-Oliver Mu̇ller, Weiqing Zheng, Di Wang, R. Dangsheng Su, Schlögl, Individual Fe-Co alloy nanoparticles on carbon nanotubes: structural and

catalytic properties, Nano Lett. 8 (2008) 2738–2743, https://doi.org/10.1021/nl8011984.

[44] W. Zheng, T.P. Cotter, P. Kaghazchi, T. Jacob, B. Frank, K. Schlichte, W. Zhang, D. S. Su, F. Schuth, R. Schlogl, Experimental and theoretical investigation of molybdenum carbide and nitride as catalysts for ammonia decomposition, J. Am. Chem. Soc. 135 (2013) 3458–3464, https://doi.org/10.1021/ja309734u.

[45] Y. Li, L. Yao, S. Liu, J. Zhao, W. Ji, C.-T. Au, Cs-modified iron nanoparticles encapsulated in microporous and mesoporous SiO_2 for CO_x-free H_2 production via ammonia decomposition, Catal. Today 160 (2011) 79–86, https://doi.org/10.1016/j.cattod.2010.02.066.

[46] J. Zhang, M. Comotti, F. Schuth, R. Schlogl, D.S. Su, Commercial Fe- or Co-containing carbon nanotubes as catalysts for NH_3 decomposition, Chem. Commun. (2007) 1916–1918, https://doi.org/10.1039/b700969k.

[47] Z.-P. Hu, C.-C. Weng, C. Chen, Z.-Y. Yuan, Catalytic decomposition of ammonia to CO_x-free hydrogen over Ni/ZSM-5 catalysts: a comparative study of the preparation methods, Appl. Catal., A 562 (2018) 49–57, https://doi.org/10.1016/j.apcata.2018.05.038.

[48] Changhai Liang, Wenzhen Li, Zhaobin Wei, Qin Xin, C. Li, Catalytic decomposition of ammonia over nitrided MoN_x/r-Al_2O_3 and $NiMoN_y$/r-Al_2O_3 catalysts, Ind. Eng. Chem. Res. 39 (2000) 3694–3697, https://doi.org/10.1021/ie990931n.

[49] J.-X. Wei, M.-Z. Cao, K. Xiao, X.-P. Guo, S.-Y. Ye, Z.-Q. Liu, In situ confining Pt clusters in ultrathin MnO_2 nanosheets for highly efficient hydrogen evolution reaction, Small Struct. 2 (2021) 2100047, https://doi.org/10.1002/sstr.202100047.

[50] J.R.Yangang Wang, Yanqin Wang, Fengyuan Zhang, Xiaohui Liu, Yun Guo, Guanzhong Lu, Nanocasted synthesis of mesoporous $LaCoO_3$ perovskite with extremely high surface area and excellent activity in methane combustion, J. Phys. Chem. C. 112 (2008) 15293–15298, https://doi.org/10.1021/jp8048394.

[51] C.J. Jia, M. Schwickardi, C. Weidenthaler, W. Schmidt, S. Korhonen, B. M. Weckhuysen, F. Schuth, Co_3O_4-SiO_2 nanocomposite: a very active catalyst for Co oxidation with unusual catalytic behavior, J. Am. Chem. Soc. 133 (2011) 11279–11288, https://doi.org/10.1021/ja2028926.

[52] I.S. Amiinu, X. Liu, Z. Pu, W. Li, Q. Li, J. Zhang, H. Tang, H. Zhang, S. Mu, From 3d zif nanocrystals to Co-N_x/C nanorod array electrocatalysts for ORR, OER, and Zn-air batteries, Adv. Funct. Mater. 28 (2018) 1704638, https://doi.org/10.1002/adfm.201704638.

[53] T. Liu, P. Zhao, X. Hua, W. Luo, S. Chen, G. Cheng, An Fe–N–C hybrid electrocatalyst derived from a bimetal–organic framework for efficient oxygen reduction, J. Mater. Chem. A 4 (2016) 11357–11364, https://doi.org/10.1039/c6ta03265f.

[54] A.L. Cazetta, T. Zhang, T.L. Silva, V.C. Almeida, T. Asefa, Bone char-derived metal-free N- and S-co-doped nanoporous carbon and its efficient electrocatalytic activity for hydrazine oxidation, Appl. Catal., B 225 (2018) 30–39, https://doi.org/10.1016/j.apcatb.2017.11.050.

[55] L. Wang, Y. Yi, H. Guo, X. Du, B. Zhu, Y. Zhu, Highly dispersed Co nanoparticles prepared by an improved method for plasma-driven NH_3 decomposition to produce H_2, Catalysts 9 (2019) 107, https://doi.org/10.3390/catal9020107.

[56] P. Xie, Y. Yao, Z. Huang, Z. Liu, J. Zhang, T. Li, G. Wang, R. Shahbazian-Yassar, L. Hu, C. Wang, Highly efficient decomposition of ammonia using high-entropy alloy catalysts, Nat. Commun. 10 (2019) 4011, https://doi.org/10.1038/s41467-019-11848-9.

[57] G. Li, H. Zhang, X. Yu, Z. Lei, F. Yin, X. He, Highly efficient Co/NC catalyst derived from ZIF-67 for hydrogen generation through ammonia decomposition, Int. J. Hydrog. Energy 47 (2022) 12882–12892, https://doi.org/10.1016/j.ijhydene.2022.02.046.

[58] J.C. Ganley, F.S. Thomas, E.G. Seebauer, R.I. Masel, A Priori catalytic activity correlations: the difficult case of hydrogen production from ammonia, Catal. Lett. 96 (2004) 117–122, https://doi.org/10.1023/B:CATL.0000030108.50691.d4.

[59] L. Xue, C. Zhang, H. He, Y. Teraoka, Catalytic decomposition of N_2O over CeO_2 promoted Co_3O_4 spinel catalyst, Appl. Catal., B 75 (2007) 167–174, https://doi.org/10.1016/j.apcatb.2007.04.013.

[60] X.-C. Hu, W.-W. Wang, Y.-Q. Wang, Q. Gu, Z. Ying, Q.-S. Jin, C.-J. Song, Jia, Co-SiO_2 nanocomposite catalysts for CO_x-free hydrogen production by ammonia decomposition, ChemPlusChem 82 (2017) 368–375, https://doi.org/10.1002/cplu.201600444.

[61] S.C. Yeo, S.S. Han, H.M. Lee, Mechanistic investigation of the catalytic decomposition of ammonia (NH_3) on an Fe(100) surface: a DFT study, J. Phys. Chem. C 118 (2014) 5309–5316, https://doi.org/10.1021/jp410947d.

[62] S. Chen, X. Chen, H. Zhang, Probing the activity of Ni_{13}, Cu_{13}, and $Ni_{12}Cu$ clusters towards the ammonia decomposition reaction by density functional theory, J. Mater. Sci. 52 (2017) 3162–3168, https://doi.org/10.1007/s10853-016-0605-1.